NTNU – Trondheim
Norwegian University of
Science and Technology

Microstructure Characterisation of Bainitic HSLA Steel for Pressure Vessels

Vanessa Valle Lopez

Chemical Engineering and Biotechnology
Submission date: June 2014
Supervisor: Jarle Hjelen, IMTE

Norwegian University of Science and Technology
Department of Materials Science and Engineering

Preface

This master thesis was done at the Institute of Material Science and Engineering at the Norwegian University of Science and Technology, NTNU, during the spring of 2014.

First of all I wish to thank my supervisor Professor Jarle Hjelen for good guidance and assistance regarding the EBSD technique and interpretation of results, throughout the semester. I would also like to thank the oil and gas company that provided the material. Senior Engineer Yingda Yu deserves a big thank you for providing vital technical guidance concerning the SEM and EBSD technique. I would also like to thank senior engineer Trygve Lindhal Schanche for help and guidance regarding preparation techniques and light microscope. A thank you also goes to Eli-Beate Larson for the help with dilatometric analysis. Staff Engineer Pål Christian Skaret also deserves a thank you for performing the tensile tests.

Declaration

I hereby declare that the work presented in this document has been performed independently and in accordance with the rules and regulations of The Norwegian University of Science and Technology (NTNU).

Trondheim, June 12.

Vanessa Valle Lopez

Abstract

The microstructure and mechanical properties in the midsection of a high thickness HSLA bainitic steel, was investigated in this master thesis. A homogeneous microstructure and good mechanical properties can be difficult to achieve in high thickness steels, due to slow cooling rates in the midsection. The different cooling rates at the surface and in the midsection of the steel can cause a difference in microstructure and mechanical properties through the thickness.

The microstructure of the base material was investigated using EBSD and light microscopy. A homogeneous bainitic microstructure was detected. The mechanical properties were investigated using Vickers hardness measurements as well as longitudinal tensile tests. The mechanical properties showed little variation and were found to be in accordance with what is common for a bainitic microstructure.

Three steel samples were heated in a dilatometer and cooled at different cooling rates in order to assess the microstructure and the mechanical properties within these cooling rates. The cooling rates were chosen to be 5 °C , 1 °C and 0,5 °C per minute. The results proved the formation of ferrite for all cooling rates and that a faster cooling rate was needed to achieve a homogeneous bainitic microstructure. A reduction in Vickers hardness with increasing ferrite content was also detected.

Sammendrag

Mikrostrukturen og de mekaniske egenskapene i midten av et bainittisk HSLA stål med stor tykkelse ble undersøkt i denne oppgaven. En homogen mikrostruktur og gode mekaniske egenskaper kan være vanskelig å oppnå i et stål med høy tykkelse grunnet den lave avkjølingshastigheten i midten av stålet. Det vil være en forskjell i avkjølingshastighet på overflaten og i midten av stålet, noe som kan føre til ulike mikrostrukturer og mekaniske egenskaper gjennom tykkelsen.

Mikrostrukturen til stålet ble undersøkt ved hjelp av EBSD og lysmikroskopi, og en homogen bainittisk mikrostruktur ble identifisert. De mekaniske egenskapene ble undersøkt ved hjelp av Vickers hardhets målinger, samt strekktester i longitudinal retning. De mekaniske egenskapene varierte lite og var generellt gode og som forventet av en bainittisk mikrostruktur.

Tre stålprøver ble varmet i et dilatometer og avkjølt ved ulike hastigheter for å undersøke hvilken mikrostruktur og mekaniske egenskaper de ulike prøvene ville få. Avkjølingshastighetene som ble valgt var 5 °C , 1 °C and 0,5 °C per minutt. Resultatene viste at ferritt hadde blitt dannet i alle prøvene og at en raskere avkjølingshastighet måtte til for å oppnå en helt bainittisk mikrostruktur. Vickers hardhetsmålinger viste minkende hardhet med økende ferritt innhold i prøvene.

Abbreviations and Symbols

Abbreviation	Explanation
$\alpha - phase$	Ferrite
$\beta - phase$	Austenite
A_1	Austenite start temperature during heating
A_3	Austenite finish temperature during heating
BCC	Body Centered Cubic
BSE	Backscattered Electrons
B_s	Bainite start temperature
CCD camera	Charge-Couple Device camera
CCT	ContinousCooling Transformation
CI	Confidence Index
EBSD	Electron Backscatter Diffraction
FCC	Face Centered Cubic
HSLA	High Strength Low Alloy
IPF	Inverse Pole Figure
IQ	Image Quality
M_f	Martensite finish temperature
M_s	Martensite start temperature
OM	Optical Micrograph
PC	Pattern centre
SEM	Scanning Electron Microscopy
WD	Working Distance

Contents

Chapter 1

Introduction

It is estimated that deepwater reservoirs represent about 10% of global oil reserves. The production from deepwater fields is also expected to increase in the coming years[18]. Many challenges arise when oil is to be produced from deepwater reservoirs, among them high pressures and temperatures. In order for the process equipment used in these deepwater reservoirs to withstand the high pressure, it needs to have large wall thicknesses. A homogeneous microstructure and good mechanical properties can be difficult to achieve in high thickness steels, due to slow cooling rates in the midsection. The different cooling rates at the surface and in the midsection of the steel can cause a difference in microstructure and mechanical properties through the thickness.

The steel investigated in this master thesis is the midsection of a high strength low alloy Cr-Mo bainitic steel, intended for use on a pressure vessel. Due to the high thickness of the steel a microstructural transformation in the midsection of the vessel can occur, where ferrite is formed and causes a reduction in mechanical properties. It is difficult to obtain a fully bainitic microstructure in Cr-Mo high thickness steel, because ferrite can precipitates from the austenite if the cooling is slow [16]. The chemical composition chosen for the steel is outside of established industrial specifications in order to improve the hardenability.

The objective of this master thesis has been to characterize the microstructure of the base material and also investigate mechanical properties. A homogeneous microstructure through the thickness was desired as well as little variation in mechanical properties. Optical microscopy, backscatter electron microscopy and EBSD were used to investigate the microstructure. The mechanical properties were tested by measuring Vickers hardness as well as looking at stress-strain curves for the steel.

Chapter 2

Theory

2.1 Steel metallurgy

Figure 2.1 shows the iron carbon equilibrium diagram, which represents the metastable equilibrium between iron and iron carbide (cementite). The part of the diagram applicable for steel is the low carbon part, up to 2% carbon [23]. At higher carbon contents the diagram is applicable for cast iron.

The diagram shows the stable phases that can be achieved if the holding time in a specific area is long enough for equilibrium to form. The steel can consist of different phases dependent on the temperature and composition. At temperatures below 723ºC the steel consists of a mixture of ferrite and cementite, with a BCC crystal structure. A transformation to FCC austenite occurs at 912ºC and at 1394ºC the austenite reverts to a BCC crystal structure, called δ – ferrite. The A_1 and A_3 lines in the diagram represent the temperatures at which there is a phase transformation at equilibrium.

By varying the cooling rates for steel annealed in the γ – region several different microstructures, not shown in the iron – carbon phase diagram, can be achieved. The phase transformations that occur can be represented by a continuous cooling transformation (CCT) diagram , as shown in Figure 2.7. The CCT diagram has a «nose» for each of the transformations from austenite to ferrite, bainite or pearlite. The hardness of the steel increases with increasing cooling rates, due to large undercooling [23]. The large undercooling leads to a hard and fine-grained microstructure.

The phase transformation temperatures in steel will vary with the amount of alloying elements, and can be found using a dilatometer. A dilatometer can measure

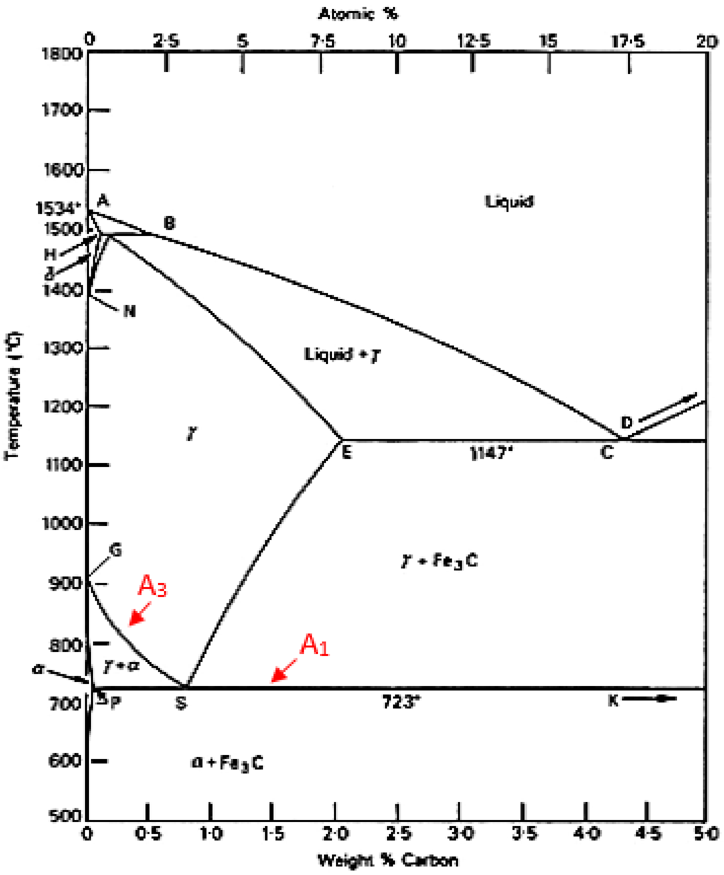

Figure 2.1: *Iron - carbon diagram.[11]*

the volumetric expansion of the steel during a thermal process. Austenite has a face centered cubic (FCC) crystal structure, whilst ferrite has a body-centered cubic (BCC) crystal structure, it will therefore be a change in volume when there is a transition from α-phase to γ-phase. During heating, steel will change its volume at a constant rate due to a constant expansion coefficient. A change in the slope of the dilatometer curve will therefore imply the beginning of the phase transformation from ferrite to austenite. A new change in the slope will occur when the steel reaches the A3- temperature and transforms from ferrite to austenite.

2.1.1 High Strength Low Alloy Steel

High strength low alloy (HSLA) steels were first developed in the 1950s to provide better mechanical properties than other steels on the market. As the name implies

HSLA steels have high strength and contains a low amount of alloying elements. These type of steels are also suitable for welding due to the low carbon content. The good combination of properties has led to their application in different industries, such as the oil and gas industry, for manufacturing of large diameter pipes and other process equipment [20]. The fine-grained microstructure of HSLA steels is achieved by controlled rolling, a process where temperature, time and the extent of deformation is predetermined. The steel is first annealed at temperatures within the austenite region, and then it goes through several rolling stages where the temperature is lowered[23]. The deformation breaks down the original coarse microstructure by repeated recrystallization of the steel. This leads to a smaller austenite grain size and formation of flow lines. Further on ferrite nucleates on both former austenite grain boundaries and flow lines during cooling and rolling. The result is a fine-grained microstructure.

2.2 The formation of ferrite

Pro - eutectoid ferrite grows by a diffusional mechanism and occurs when low carbon steel (up to 0,8 % carbon) is cooled to temperatures under or close to equilibrium conditions. The pro - eutectoid ferrite can exist in two different forms, dependent on grain size and cooling conditions. These two forms are allotriomorphic ferrite, which nucleates at prior austenite grain boundaries and Widmanstatten ferrite which is formed close to the A3 temperature [2].

Allotriomorphic ferrite forms if the austenite grains are small or the cooling is slow [23]. As mentioned before this type of ferrite nucleates at the austenite grain boundaries and grows both along the grain boundaries and into the austenite grains. At greater cooling rates Widmanstatten ferrite, which consist of plates or laths, will form [11]. Primary Widmanstatten ferrite grows from the austenite grain surfaces and secondary Widmanstatten ferrite nucleates at allotriomorphic ferrite already present in the microstructure. In Figure 2.2 the morphology of primary and secondary Widmanstatten ferrite can be seen.

The growth rate of ferrite depends on how fast alloying elements partitioned during transformation diffuse ahead of the moving interface and also on the intrinsic mobility of the austenite-ferrite interface [2].

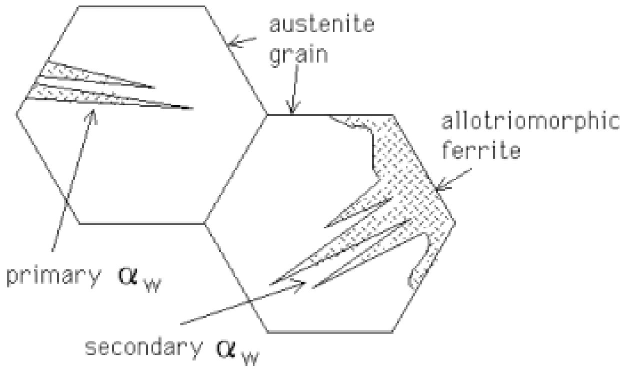

Figure 2.2: *The morphology of primary and secondary Widmanstatten ferrite [4].*

2.3 The formation of bainite

Edgar Bain was the first to discover bainite during his studies of the isothermal decomposition of austenite. Bainite occurs in the temperature range of 250-550ºC, during cooling rates too fast for pearlite to form, but to slow for the formation of martensite. Depending on the transformation temperature, bainite can exist in two different forms: upper and lower bainite [11]. Both forms consist of aggregates of plates of ferrite, separated by untransformed martensite, austenite or cementite [3]. The plates grow in clusters called sheaves and the plates within each sheaf are called the sub-units, which are of identical crystallographic orientation and often separated by low-misorientation boundaries. The growth of the plates involves a shape change and can be described by an invariant plaine strain with a large shear component. Due to the shear component the surrounding austenite deforms plastically and increases the dislocation density so that the growth of the bainite sub-units eventually stops.

Figure 2.3 illustrates the difference in the formation of upper and lower bainite. Upper bainite forms at temperatures between 550-400ºC, where the diffusion of carbon is too rapid for precipitation of carbides in the ferrite. Lower bainite forms at temperatures between 400-225ºC, where the diffusion of carbon goes slowly and some of the carbon has an opportunity to precipitate as fine carbides in the ferrite. The difference in formation of lower and upper bainite leads to different mechanical properties. Lower bainite is found to be tougher than upper bainite and possesses a much higher strength, due to the precipitation of carbides inside the plate structure. The coarse cementite particles between the ferrite plates in upper bainite act as a starting point for fracture.

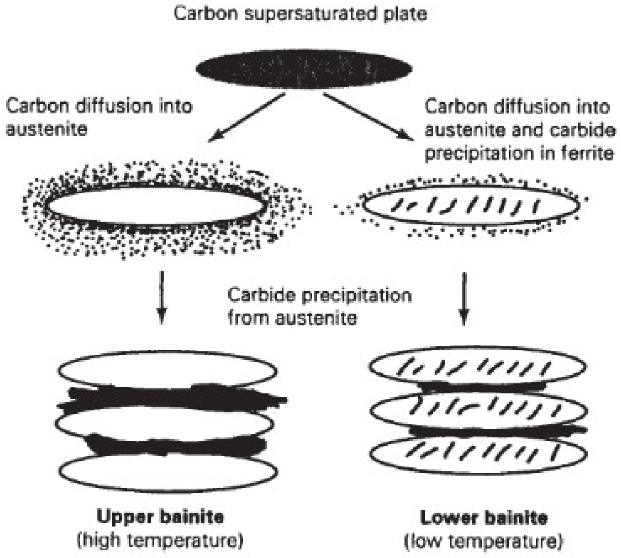

Figure 2.3: *The formation of upper and lower bainite[11].*

In order to obtain a fully bainitic microstructure the optimum combination of alloying elements must be used, as the bainitic C - curve is overlapped by those of ferrite and pearlite [30]. It is even more difficult to obtain a fully bainitic microstructure in Cr-Mo steel of thickness over 300 mm because ferrite precipitates from the austenite during slow cooling caused by the steel thickness [16].

2.3.1 Role of alloying elements

There is a bainite-start temperature, Bs, over at which bainite cannot form. The bainite-start temperature is highly dependent on the amount of alloying elements in the steel, as can be seen from Equation (2.1) [11], where the concentrations are given in weight percent.

$$B_s(^{\circ}C) = 830 - 270C - 90Mn - 37Ni - 70Cr - 83Mo \tag{2.1}$$

Carbon has the greatest influence on the range of temperature over which upper and lower bainite occur. This comes from the fact that carbon has a much larger solubility in austenite than in ferrite and acts as an austenite stabilizer, which leads to a retardation of the reaction kinetics [11].

Most alloying elements will depress the Bs temperature and also usually result in the retardation of the ferrite and pearlite reactions, leading to a greater separation of the pearlite and bainitic reactions. A fully bainitic microstructure is however still difficult to obtain because of its proximity to the martensite reaction. Figure 2.4 shows the effect of alloying elements on the bainite TTT curve. Notice that the pearlite and ferrite "noses" are pushed back so that bainite can form more easily.

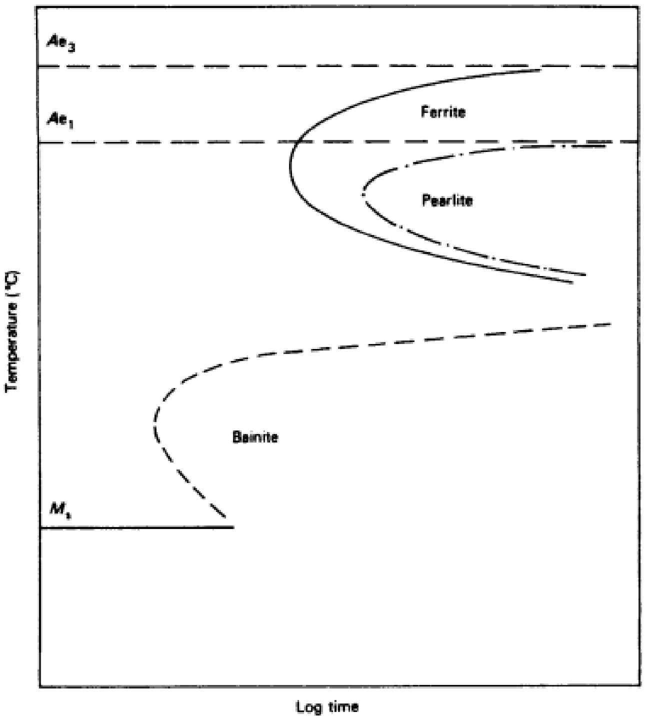

Figure 2.4: *The effect of alloying elements on the bainite TTT curve for a low-alloy steel [11].*

2.3.2 How to distinguish bainite from other microstructures in EBSD

EBSD can be a great technique to use when characterizing different microstructures, although it can be limited when dealing with complex microstructures and difficulties in achieving reliable data can occur. Microstructures having different crystallographic structure can rather easily be separated by using EBSD, but microstructures with the same crystal symmetry can be difficult to separate [29]. Difficulties in characterising a microstructure using EBSD can occur if the microstructure contains a large amount of dislocations and sub-grain boundaries, leading to a distorted Kikuchi Pattern [27].

Bainite contains a large amount of dislocations and is crystallographically identical to ferrite; they both have the BCC crystal structure. In previous works the two phases have been separated using a variety of different methods. WU et.al [27] distinguished the phases by looking at the degree of lattice imperfection using the Image Quality (IQ) values. Zaefferer et.al [28] used Grain Reference Orientation deviation maps (GRO) and Kernel Average Misorientation maps (KAM), as well as Image Quality maps in order to find areas with larger geometrically necessary dislocation density. Ryde [21] used the averaged IQ value of each grain and selected a threshold in order to differentiate between bainite, martensite and ferrite. Bainite contains a larger amount of lattice defects than ferrite and this leads to lower IQ and CI values, due to unclear diffraction bands. Bainite also contains a large amount of sub – grains which can be detected using EBSD. Ferrite on the other hand contains a low dislocation density and no sub - grains.

2.4 The formation of martensite

The formation of martensite can occur when a steel is quenched from the austenite region to room temperature. Martensite formation is often referred to as a diffusionless shear transformation. This means that martensite forms by a deformation of the austenite lattice without diffusion of atoms, which causes a shape change of the transformed region. The martensite formation does not start before a certain temperature, called the martensite-start temperature (M_S), is reached. The fraction of transformed martensite does not depend on time, but on the undercooling below M_S [3]. Martensite has many similarities with bainite, the main difference is however that in bainite the carbon is precipitated as carbides [23].

The athermal reaction character of martensite is caused by the rapid nucleation and growth, leading to the fraction transformed being only dependent on the number of active nucleation sites. The number of nucleation points will again depend on the driving force for transformation provided by the undercooling.

Various equations for the M_s temperature have been developed, but the most commonly used is the equation represented below, where the concentration of the elements is in weight percent [23].

$$M_s(^\circ C) = 539 - 423C - 30,4Mn - 17,7Ni - 12,1Cr - 7,5Mo \qquad (2.2)$$

2.5 Mechanical properties of different microstructures

The mechanical properties of steel will vary with the microstructure it possesses. There is a wide variety of microstructures possible, all with numerous mechanics contributing to their mechanical properties.

2.5.1 Ferrite

Only a few commercial steels are completely ferritic, because the ferritic microstructure is relatively soft and ductile. Ferrite has a BCC crystal structure and the mechanical properties are strongly dependent on grain size. Strengthening of the microstructure can be done by solid solution strengthening, refinement of grain size and precipitation strengthening [11]. The influence of solid solution elements on the yield strength of ferrite can be seen in Figure 2.6. The toughness can, as mentioned, be increased by refinement of grain size, but a smaller grain size will lead to a larger amount of pearlite being nucleated. An increased pearlite content will decrease the toughness.

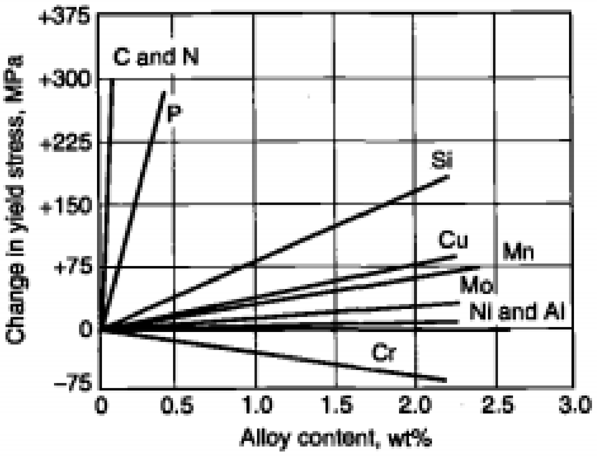

Figure 2.5: *The influence of solid solution elements on the changes in yield strength of low-carbon ferritic steels [19].*

2.5.2 Bainite

Bainitic steels have a favourable combination of toughness, strength and formability, they are therefore often used in pipes and other process equipment in the oil and gas industry [20]. The highest ever combination of strength and toughness have been obtained in bainitic steels. There are several factors contributing to the strength of bainite, the most important are the intrinsic strength of pure annealed iron, substitutional solid solution strengthening, strengthening due to carbon in solid solution and a variety of microstructural components like dislocation strengthening, particle effects and grain size effects [3]. As shown in Figure 2.6 the strength of bainite increases linearly with decreasing transformation temperature. Note the rapid increase in tensile strength as the transformation temperature decreases.

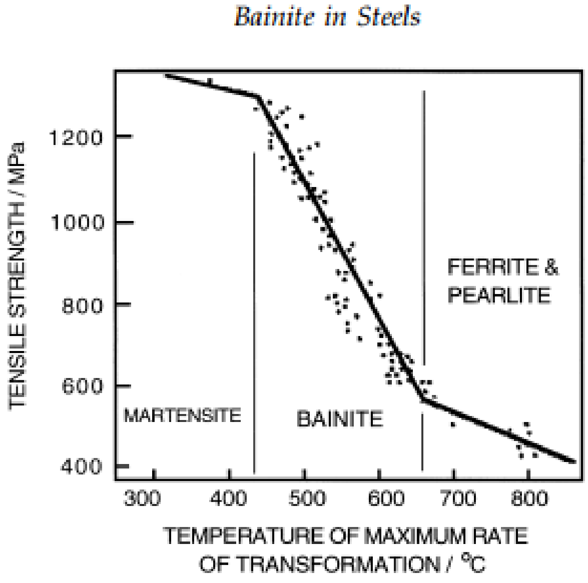

Figure 2.6: *Relationship between transformation temperature and tensile strength of martensite, bainite, and ferrite-pearlite [3].*

The mechanical properties of bainitic steels are strongly dependent on the microstructural morphology and composition. Yield strength can range from 450 to 950 MPa and tensile strength from 530 to 1200 MPa [6]. Low-carbon bainitic steels also show superior tensile ductility compared to other high-carbon steels [3]. The ductility of a bainitic steel can be improved by reducing the carbon concentration, the strength can be maintained by using substitutional solid solution strengthening. In order to achieve a bainitic microstructure over a wide range of transformation temperatures, a special chemical composition is needed, for example 1/2Mo-B steel. The CCT diagram for this steel can be seen in Figure 2.7.

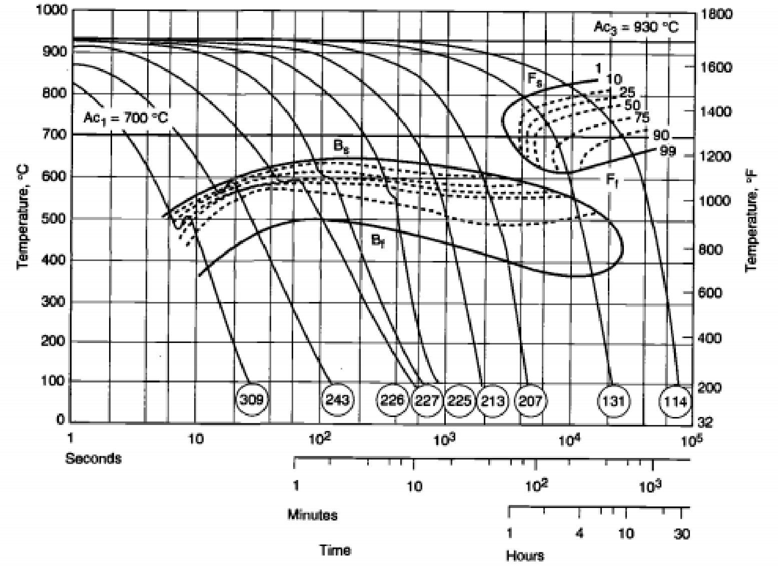

Figure 2.7: *CCT diagram of a 1/2Mo-B steel. Composition is 0.093% C, 0.70% Mn, 0.36% Si, 0.51% Mo, 0.0054% B. The numbers in circles indicate Vickers hardness after cooling to room temperature [26].*

It is shown that the hardness of bainite increases linearly with carbon concentration, by approximately 190 HV per wt%[13]. The hardness of fully bainitic microstructures is also insensitive to both the austenite grain size and the austenitising temperature [15]. This is due to the size of the bainite sub-units.

2.5.3 Martensite

Martensite is a high strength microstructure, where the relationships between strength, toughness and microstructure are yet to be fully understood. The microstructure contains high densities of dislocations and fine twins. There are several mechanisms contributing to the strength of martensite [11]:

- Interstitial and substitutional solid solution
- Fine plate and lath structure (many grain boundaries)
- Dislocation strengthening
- Segregation of carbon atoms

- Precipitation of carbides in tempered martensite

Most alloying elements will lower the M_s temperature, therefore the strength of martensite in alloy steels are usually higher than in plain carbon steels. The lower M_S temperature leads to less auto-tempering during cooling. From equation 2.2 it can clearly be seen that carbon is the alloying element having the strongest impact on the M_S temperature. The effect of carbon on the M_s and M_f temperature is shown in Figure 2.8 The effect of carbon on the hardness of martensite and austenite can be seen in Figure 2.9.

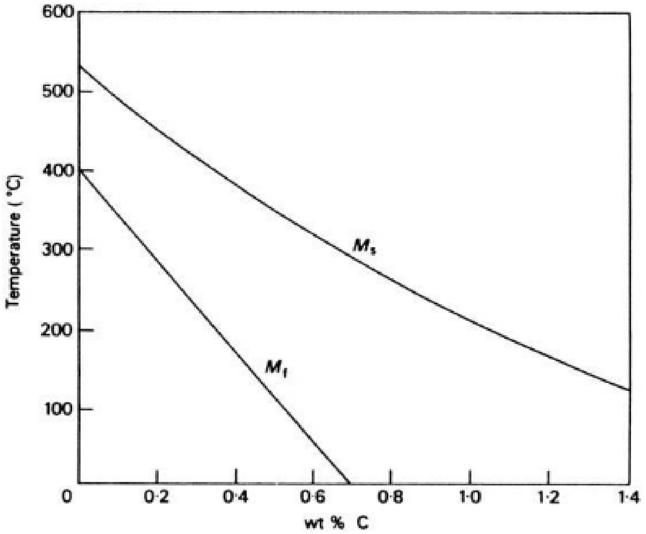

Figure 2.8: *The effect of carbon concentration on M_s and M_f [11].*

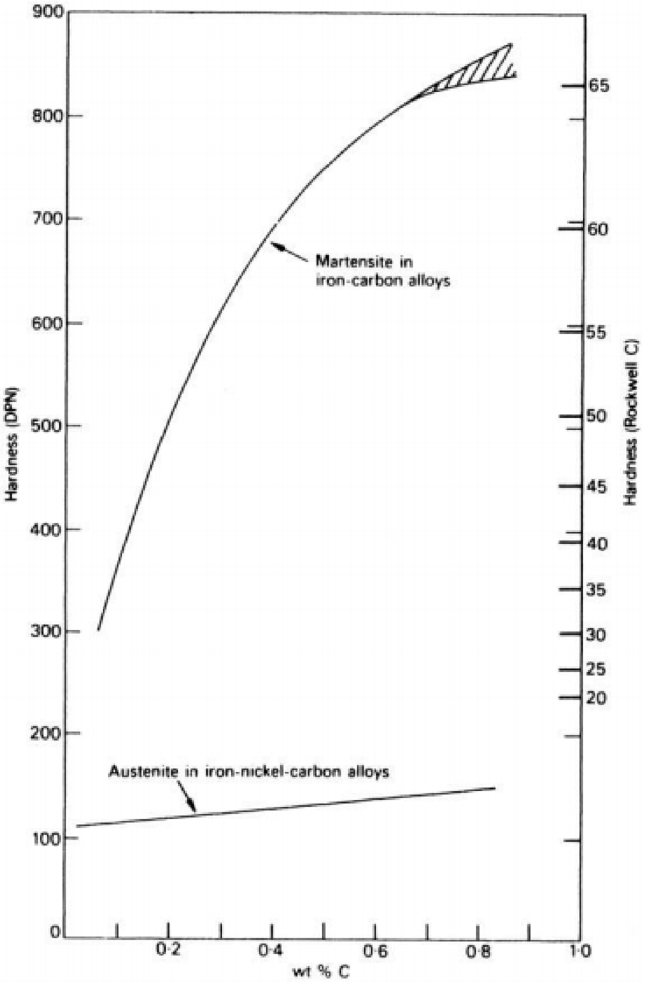

Figure 2.9: *The effect of carbon concentration on the Rockwell hardness of martensite and austenite[11].*

2.6 Hardenability

The ability of steel to form martensite on quenching is refereed to as the hardenability. If a steel has little hardenability, it means that a large cooling rate is needed in order to harden the steel. There are mainly two variables effecting the hardenability of a steel; alloying elements and grain size [7]. Nearly all alloying elements increase the hardenability by pushing the ferrite/perlite "nose" in the CCT diagram toward longer times [23]. The hardenability also increases with increasing austenite grain size, due to a reduction in grain boundary area. The reduced grain boundary area leads to fewer nucleation sites for pearlite and ferrite, and therefore these transformations are slowed down.

Industrial components often have large cross sections, leading to difficulties if the component is to be through hardened. The cooling rate at the surface of the component will be higher than in the center, which can cause differences in microstructure and properties through the cross section of the component. The cooling rate in the center should therefore be the one considered if the component is to be through hardened. The variation in cooling rate between the surface and centre of an oil-quenched 95 mm diameter steel bar is illustrated in Figure 2.10. The centre cooling curve intersects the bainite region and the surface cooling curve does not, the steel bar is therefore expected to have a bainitic core and a martensitic surface.

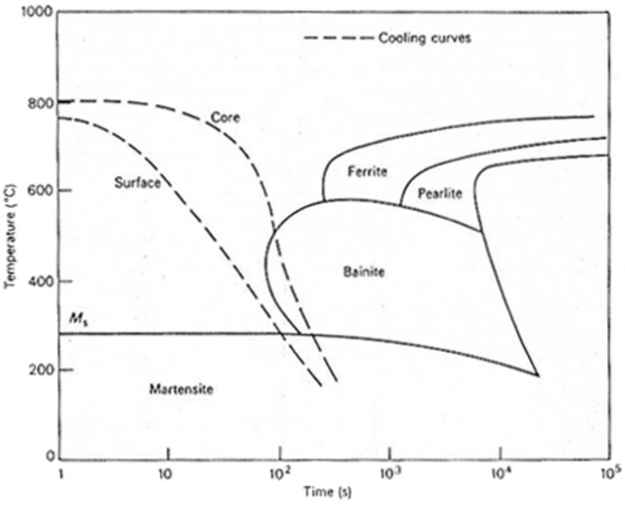

Figure 2.10: *Relation between cooling curves for the surface and core of an oil-quenched 95 mm diameter bar and their effect on microstructure [25].*

2.7 Sample preparation

In order to obtain high quality electron backscatter diffraction patterns (EBSP's), surface sample preparation is important. A well prepared sample surface is essential because the EBSD-technique is dependent on analytical signals from the top 20 nanometres of the specimen [22]. Surface contamination or deformation, results in EBSD patterns of poor quality and will affect the accuracy of the results during material analysis.

For a sample to be suitable for examination in SEM and EBSD, the top 100 nm of the sample needs to be crystalline and free from excessive plastic deformation

[10]. Deformation can occur both during cutting and mechanical polishing. There are several techniques used to get a deformation free surface, but the main three methods are electropolishing, chemical mechanical polishing and ion milling. After both chemical mechanical polishing and electropolishing a final cleansing step, using plasma cleaning can be necessary.

2.7.1 Chemical mechanical polishing

Chemical mechanical polishing can be a good way to get a deformation free surface. The method is partly mechanical and partly chemical. The sample surface reacts with the active oxide suspension and forms a brittle reaction layer on the surface. The reaction layer is removed by the small abrasive particles in the suspension [24]. There are many active oxide polishing suspensions to choose from, but Struers OP – S is found to give good results in removing the deformation layer from iron samples [24].

2.7.2 Plasma cleaning

The plasma cleaner removes contamination from the sample surface by using a reactive gas formed by the plasma. The cleaning is done without changing the specimens composition or structural characteristics [14]. Plasma cleaning also prevents contamination during EBSD scanning.

2.8 Electron Backscatter Diffraction

Electron Backscatter Diffraction (EBSD) is a technique used to examine the crystallographic orientation of crystalline and polycrystalline materials in a scanning electron microscope (SEM). EBSD can be used to determine grain orientations, local texture and grain boundaries in addition to phase identification and distribution [22].

The collection of an EBSD pattern is done by sending a beam of electrons on a tilted crystalline sample in the SEM. The electrons hit the surface of the sample and interact with the atomic planes in the specimen surface, before they hit a phosphor screen and forms a diffraction pattern. The diffraction pattern is characteristic of the samples crystal structure and orientation, and appears as an arrangement of nearly parallel bright band edges on a flat surface,as illustrated in Figure 2.11. The phosphor screen is located approximately two cm away from the specimen [22].

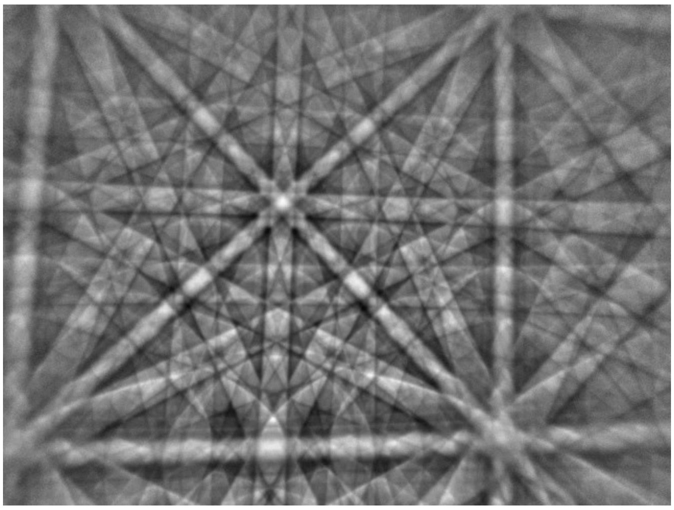

Figure 2.11: *Kikuchi pattern from a nickel sample [12].*

In order to detect a large amount of backscattered electrons, the sample needs to be tilted relative to the electron beam. The number of backscattered electrons increase with the tilt angle. An angle of 70º is typical during recording of EBSD patterns [17]. The relative position of the objective lens, the tilted specimen and the phosphor screen is illustrated in Figure 2.12.

Diffraction of the backscattered electrons occur according to Bragg's law:

$$2d_{hkl}\sin(\theta_B) = n\lambda \tag{2.3}$$

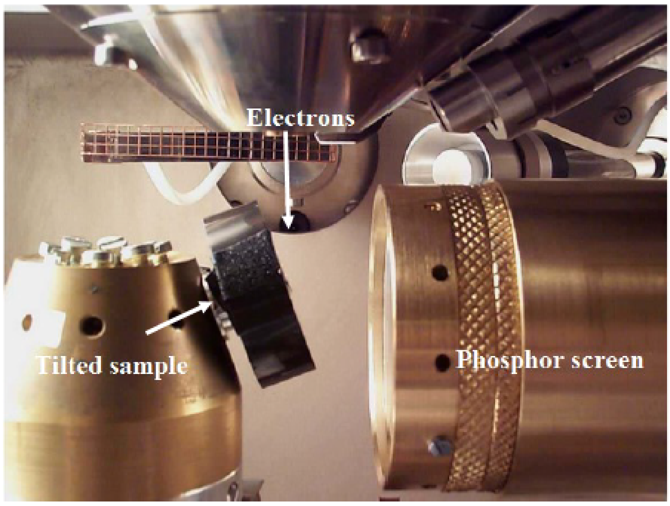

Figure 2.12: *Typical setup for EBSD in SEM [10].*

where d_{hkl} is the interplanar spacing, θ_B is the Bragg angle and λ is the wavelength of the incident electron beam. n is the order of reflection and is set to 1 in EBSD [9]. The interplanar spacing of a cubic crystal can be found from the following equation:

$$d = \frac{a_0}{\sqrt{h^2 + k^2 + l^2}} \tag{2.4}$$

where a_0 is the lattice parameter and h,k,l the Miller indices for the given atomic plane.

The diffraction pattern appears, as mentioned before, as nearly parallel bright bands on a flat surface, also called Kikuchi bands, as shown in Figure 2.11. In theory the diffracted electrons form sets of high angular cones with the angle 180-$2\theta_B$ for each diffracted plane, as presented in Figure 2.13. The Bragg angle is small in EBSD, which makes the cone radius big compared to the phosphor screen. The cones form two nearly parallel bright lines with the distance $2\theta_B$ on the screen, but they appear as straight lines.

The centreline of each Kikuchi band represents an atomic plane, whilst the intersection point between two Kikuchi – bands represents a crystal orientation in the material. Because the backscattered electrons interfere with several atomic planes, the diffraction pattern will consist of several bands.

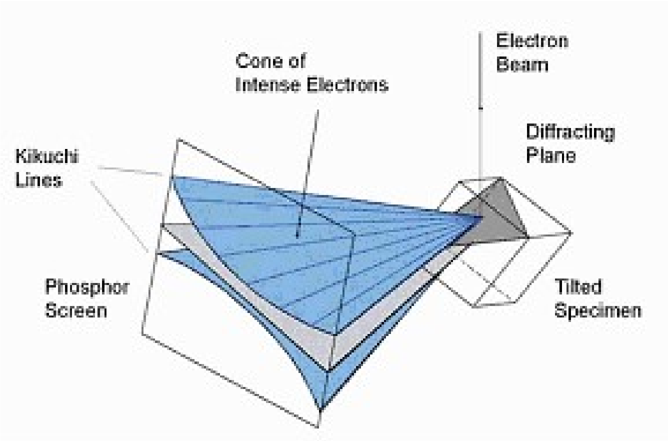

Figure 2.13: *Sketch of the diffracting cones [22].*

2.8.1 Parameters in EBSD

A Charge Couple Device (CCD) camera and a control system for the sample and electron beam makes it possible to scan large areas of a sample. Figure 2.14 shows a sketch of a typical EBSD set up. The CCD – camera records the Kikuchi patterns from the backscattered electrons and transfer the bitmap image to a computer. A signal is subsequently sent to the SEM, and the electron beam is moved one-step length according to the settings. A new pattern is recorded every time the electron beam moves along the sample surface, until the scan is complete.

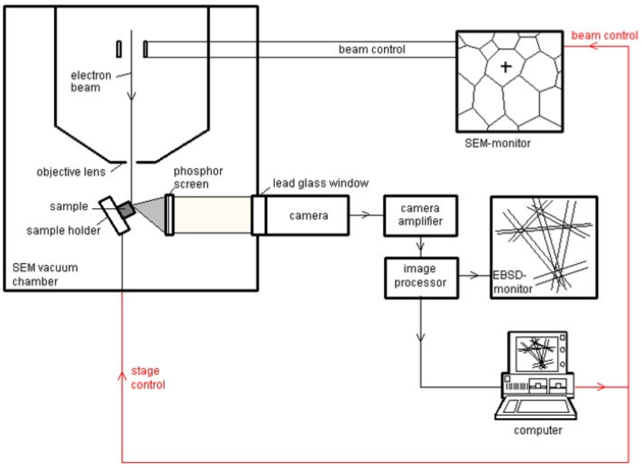

Figure 2.14: *Scheme of a typical EBSD set-up [10]*

In order to achieve good Kikuchi patterns, fast, the signal/noise ratio during acquisition needs to be high. To increase the ratio, a long exposure time or a high beam current can be used. An increase in exposure time will also increase the time it takes to scan an area. The beam current can be increased by increasing the aperture in the SEM, but then there will be a decrease in spatial resolution due to an increase in electron beam size [5].

The acceleration voltage is another important parameter to control. The acceleration voltage affects the wavelength of the incident electron beam. An increase in acceleration voltage leads to a decrease in wavelength and narrow Kikuchi bands. As a consequence of Braggs law, given in equation (2.3), the width of the Kikuchi bands are proportional to the wavelength of the electron beam. Narrow Kikuchi bands makes it easier to locate the center line, but the disadvantage with high acceleration voltage is an increase in excitation volume due to deeper electron penetration. The increased excitation volume leads to a decrease in spatial resolution. An acceleration voltage of 20 KV is normally used on samples with high atomic numbers [9].

The step size influences the amount of indexed points in EBSD. A small step size can increase the noise close to the grain boundaries, whilst a large step size will give a coarse scan [5]. The optimum step size is according to Chen et.al dependent on the magnification and decreases with increasing magnification, as shown in Figure 2.15.

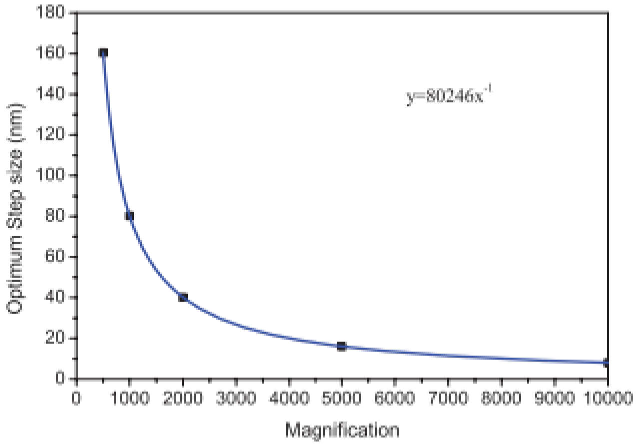

Figure 2.15: *Optimum step size as a function of magnification [5].*

To reduce the path length of the backscattered electrons, the specimen can be tilted and the working distance (WD) adjusted. When the working distance is adjusted, the pattern center will move up and down on the phosphor screen and the fraction of indexed points can be reduced [5]. The effect of working distance on the indexed points is shown in Figure 2.16.

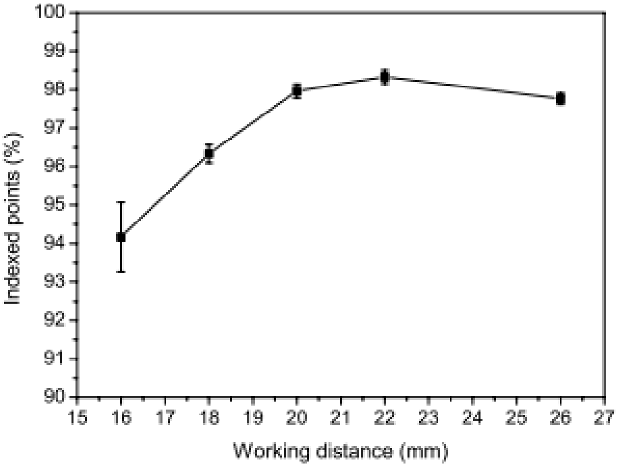

Figure 2.16: *Fraction of indexed points as a function of working distance in a coarse grained Ti sample [5].*

2.8.2 TSL OIM Data collection

The TSL OIM Data collection 5.32 software is used to index the diffraction patterns from the scan. This is needed to collect information about the crystallographic orientations and phase distributions in the sample. The crystallographic orientation can be calculated from the position of the Kikuchi bands, which can be found by using the Hough transform. The Hough transform, transforms the Kikuchi - bands from the xy – space to become points in the Hough – space (ρ,ϑ). A pixel in the xy space is transformed into a sinusoidal curve according to equation (2.5) [8].

$$\rho = x\cos(\theta) + y\sin(\theta) \tag{2.5}$$

Several pixels on a line in the xy space, produces different sinusoidal curves that intersect in a point in Hough space, as shown in Figure 2.17.

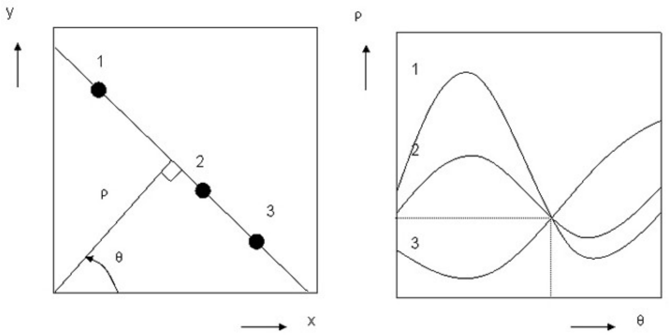

Figure 2.17: *Illustration of how several pixels in the xy - space are transformed to a point in Hough space [8].*

The diffraction patterns are then indexed by using the geometry of the bands to find the corresponding orientation.

In order to get a correctly indexed diffraction pattern, the Pattern Center (PC) needs to be calibrated properly. The pattern center is defined as the point on the phosphor screen with the shortest normal distance to the focus point on the sample. The PC is expressed with xyz – coordinates, where x and y gives the position of the PC on the phosphor screen and z gives the distance to the sample surface. The position of the Pattern Center is determined by a iteration process, where the user propose a position for the PC and the software tunes the coordinates based on various pattern quality parameters . TSL OIM Data collection uses the three parameters Confidence Index (CI), Fit and Image Quality (IQ) to estimate how good the quality of the scan is.

The confidence index indicates how accurate the calculation of the crystal orientation is. This is done by listing all the possible band triplets and compare them to the different indexed solutions. CI can be defined as the difference in amount of votes between the two best solutions, divided by the total number of votes from the band triplets, as shown in the following equation:

$$CI = \frac{V_1 - V_2}{V_{ideal}} \tag{2.6}$$

where V_1 and V_2 are the number of votes for the best and second best solution and V_{Ideal} is the total number of possible votes from the band triplets. The CI value varies between 0 and 1, where a value near 1 indicates a high probability that the orientation is correctly indexed.

The Fit – value is the angle deviation between the calculated band and the detected band. A low Fit value represents good agreement between bands in the pattern and the chosen orientation.

The Image Quality value describes the average height of the peaks in the Hough transform. The quality of each diffracted point can be imaged in an IQ map. An IQ map is a black and white picture where bright areas refers to high IQ values and black or dark areas represent low pattern quality. Low pattern quality may be due to impurities on the sample surface, microstructure, grain boundaries, among others.

2.8.3 TSL OIM Data analysis

In TSL OIM Data Analysis 6.1, the indexed EBSP's from TSL OIM Data Collection 5.32 can be used to analyse and visualize grains, phases and crystal orientations present in the material. It is important to note that this is a very large program with functions beyond the scope of this work. The program can give information in the form of pole figures and maps. The three most common maps are inverse pole figure (IPF) map, phase map and Image Quality (IQ) map.

In an inverse pole figure map each point from the OIM scan is coloured according to some parameter reflecting the crystallographic rotation. In Figure 2.18 an IPF map can be seen, where the colours correspond to the crystal orientations shown in the projection. Crystals with their 101 axis normal to the surface of the sample will be green, and so on.

The Image Quality map shows the quality of each diffracted point, as mentioned before. In the IQ map you can see particles, adhesive stripes, areas with higher

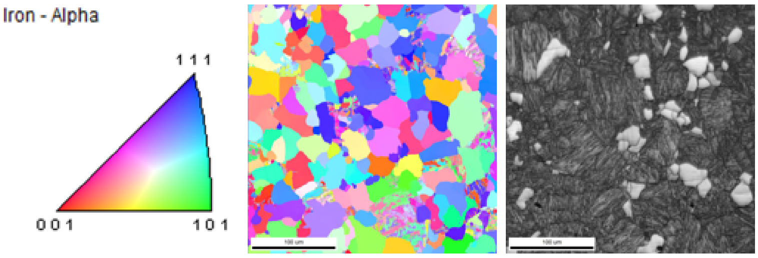

Figure 2.18: *a) Inverse Pole Figure map, where crystals with their 101 axis normal to the surface of the sample will be green and b) IQ map of sample containing many dislocations.*

dislocation density, as these will have lower image quality, among others. In Figure 2.18 b) an IQ map with a microstructure containing many dislocations can be seen.

Chapter 3

Experimental

3.1 The material

The steel that has been investigated in this thesis is a high strength low alloy steel, with a bainitic microstructure. The steel is quenched and tempered and has the chemical composition given in Table 3.1. The chemical composition was found by Sintef Molab using a spark eroder.

Table 3.1: *Chemical Composition of steel, values are in wt%.*

C	Si	Mn	P	S	Cr	Ni	Al	Cu	Mo	Nb	V	Ti	Co	B+N
0,21	0,22	0,53	0,006	0,001	2,50	0,45	0,021	0,12	1,04	0,005	0,052	0,002	0,012	0,0081

3.2 Dilatometric Analysis

As explained in section 2.1 of the theory a dilatometer can measure the volumetric expansion of the steel during a thermal process. During heating, steel will change its volume at a constant rate due to a constant expansion coefficient. A change in the slope of the dilatometer curve will therefore imply the beginning of the phase transformation from ferrite to austenite. A new change in the slope will occur when the steel reaches the A3- temperature and transforms from ferrite to austenite.

Three steel samples (11mm X 11mm X 3mm) were heated to a peak temperature of 950 °C, in a Netzsch DIL 402 C, with a heating rate of 2 °C per minute and holding time of ten minutes. The three steel samples were cooled from 950ºC to room temperature with different cooling rates in order to assess the microstructure and the mechanical properties formed. The cooling rates were chosen to be 5 °C , 1 °C and 0, 5 °C per minute, where 5 °C per minute was the fastest cooling rate possible for the dilatometer used. In addition the transformation temperature from austenite to ferrite and bainite was found from the dilatometer results.

3.3 Sample geometry

The different samples were cut from the steel block using a water cutter. A water cutter was chosen because it gives minimal deformation of the material and prevents heat formation, so that the mechanical properties are maintained.

Samples for dilatometer, hardness testing and EBSD needed to have different geometries. For hardness measurements a rod with a length of 111mm, representing the entire thickness of the steel was cut out. The geometry of the sample can be seen in Figure 3.3. The dilatometer samples needed to be small in order to fit in the apparatus and had a thickness of 3 mm. The samples from the base material, that were going to be investigated in EBSD, was 10x10x10 mm.

3.4 Mechanical Testing

3.4.1 Tensile testing

Tensile testing was performed by an engineer at NTNU on a MTS 810 universal testing machine. A strain rate of 2mm/min with a load cell of 100KN was used. The extensometer was 25 mm. Three 8mm long tensile test specimens were machined from the longitudinal direction of the steel block. Tension tests were not done in transversal direction due to insufficient amount of material. One of the tensile test specimens was grinded and polished before tensile testing was done, in order be able to investigate the fracture in EBSD. In Figure 3.1 the three tensile test specimens are shown.

Figure 3.1: *Picture of the three tensile test specimens.*

3.4.2 Hardness testing

A specimen rod, as shown in Figure 3.3, was extracted from the received steel block. The rod represented the whole thickness of the steel block, so that hardness measurements could be done through the thickness, from inner to outer diameter. The specimen rod was grinded using Struers MD Piano grinding discs 80,220,500,800 and 1200. After grinding, the specimen was polished using Diapro Nap and Dap polishing discs.

Vickers hardness was measured on a Struers Duramin - A2500, shown in Figure 3.2, with 5 kg force. Three parallel measurements, 3 mm apart, were done every 5 mm until inner diameter was reached. In total 20 parallels and 60 hardness measurements were done. A schematic drawing of the rod with hardness measurements can be seen in Figure 3.3.

Hardness measurements were also done on the dilatometer specimens, but here only three measurements with three parallels could be done due to the size of the specimens.

Figure 3.2: *Picture of the Struers Duramin - A2500 used for measuring Vickers hardness.*

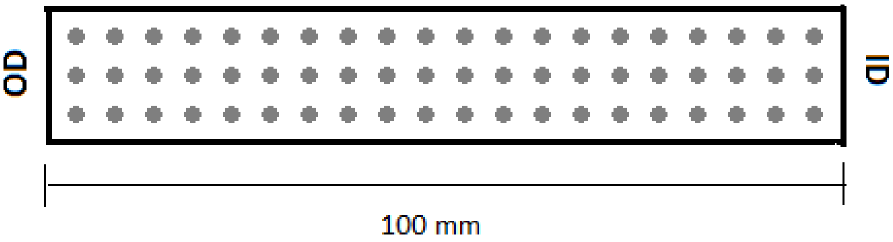

Figure 3.3: *Schematic drawing of the positions of the hardness measurements.*

3.5 Sample preparation

A well prepared sample surface is essential in order to obtain high quality electron backscatter diffraction patterns (EBSP's). All the steel samples in this assignment were prepared manually. Manual preparation was chosen because automatic preparation requires the samples to be moulded into Struers ClaroCit during grinding. The mould needs to be removed from the sample before investigation in the SEM, this can be difficult without leaving residues which can cause charging of the sample. Sample deformation can also be introduced during removal of the mould.

In her project thesis the author tested several specimen preparation techniques and found that chemical mechanical polishing gave the best result for specimens intended for investigation using EBSD. The same preparation technique was used in the current master thesis.

The samples were wet grinded manually using the following grinding discs; 80, 320, 500, 800, 1000, 1200 and 2400. Between each grinding step, the samples were cleaned with water and ethanol in order to remove residues from the previous step.Final polishing was done according to Table 3.2.

Table 3.2: *Polishing Steps.*

Step	*Dispersion*	*Garin Size*	*Time*
1	Diapro Dac	3	10 min
2	Diapro Nap	1	10 min
3	OP-S	0,04	4-10 min

The time spent on chemical mechanical polishing could not be the same for all the samples due to different microstructure. The base material and the dilatometer sample cooled at 5 °C per minute were polished with OP-S for 10 minutes. The two samples cooled at 1 °C and 0, 5 °C per minute could not tolerate 10 minutes of polishing with OP-S. The optimal polishing time for these two samples were found to be 4 minutes.

In order to remove any residues from the grinding and polishing, the samples were submerged in an ultrasonic bath, containing acetone for 10 minutes after final polishing. The samples were then cleaned in ethanol in order to remove remaining acetone from the ultrasonic bath.

All the samples were cleaned in Fishione 1020 Plasma Cleaner for 5 minutes before every EBSD investigation. The plasma cleaner removes any remains of contamination and prevents contamination from occurring during imaging [14]. After this step the samples were handled with rubber gloves in order to avoid stains and contamination from fingertips.

3.6 SEM

The scanning electron microscope applied was a Hitachi SU - 6600 FESEM. The microscope is a Field Emission Scanning Electron Microscope (FESEM). The EBSD – detector was a NORDIF UF – 1000 and the software that was used to acquire and save the EBSD patterns, was NORDIF 1.4.0. The system was off - line and saved all the diffraction patterns on a hard drive for later indexing. A picture of the SEM can be seen below.

Figure 3.4: *The Hitachi SU-6600 FESEM.*

3.6.1 BSE

The three samples that had been heated and cooled in a dilatometer was investigated using Backscatter Electron imaging (BSE) as well as EBSD.

The working distance for BSE imaging was chosen to be 10 mm. When the working distance was set, focus and astigmatism needed to be carefully tuned in order to be able to see the two different phases in the samples. The probe current needed to be low in order to have a good resolution, it was therefore chosen to be between 5 - 15 nA. This was done in SE mode. After the settings were correct, the mode was changed from SE to BSE and imaging was done. The settings used for BSE imaging are represented in Table 3.3.

Table 3.3: *BSE - settings.*

Settings	*Values*
Accelerating voltage	15KV
Probe current	10 - 12 nA
Magnification	500 - 5000X
Working Distance	10 -11 mm

3.6.2 EBSD

Focus, position of electron beam and astigmatism needed to be correctly tuned before tilting and EBSD scanning could be done. The beam current was also adjusted. The settings used are presented in Table 3.4.

Table 3.4: *SEM - settings*

Settings	*Values*
Accelerating voltage	20KV
Probe current	High Current Mode
Magnification	300X - 1000X
Tilt Angle	70º
Working Distance	25 - 26,5 mm
Dynamic focus	35-50

After the sample was tilted, an appropriate working distance was set and the dynamic focus was carefully tuned. A representative area of the specimen was found in the SEM and the surface area was scanned into the NORDIF 1.4.0 software. Magnification, accelerating voltage, working distance and tilt angle were written into the NORDIF software, before the EBSD scanning was done. To optimize the pattern quality and acquisition speed, settings for both calibration and acquisition were changed. The quality of the calibration patterns needs to be good, they therefore have a higher resolution and longer exposure time than the acquisition patterns. One EBSD scan with the chosen settings, seen in Table 3.5, took 33 minutes.

To prevent the picture from being overexposed the binning needed to be calibrated. A resolution of 160 X 160 was chosen for the pattern images, which corresponds to a 3 X 3 binning, meaning that the CCD – camera becomes 9 times more sensitive to light and the pattern image is reduced by a factor of nine. The gain can also be adjusted in order to increase the intensity of the pattern image, but increasing the gain will also increase the noise in the image. This is however not a big problem as the Hough transform is insensitive to noise.

Before the EBSD scan was recorded, background subtraction was done in order to increase the contrast in the diffraction picture. Nine calibration patterns and one acquisition pattern from the chosen area were selected. Two calibration patterns were recorded in each corner of the scanning area and one in the middle, in order to find the pattern center during indexing. The acquisition point was recorded in the center of the scanning area in case of a bad quality scan.

Table 3.5: *Acquisition, calibration and region of interest settings in NORDIF 1.4.0.*

Acquisition settings	
Frame rate	400 fps
Resolution	160 X 160
Gain	0-5
Calibration settings	
Frame rate	100 - 150 fps
Resolution	240 X 240
Gain	0-3
Region of interest	
Height	100 - 300 µm
Width	100 - 300 µm
Step size	0,100 - 0,300 µm

3.6.3 Indexing

Indexing of the diffraction patterns was done using TSL OIM Data Collection 5.32. The crystal structure expected to be found in the steel samples was BCC, the α - iron was therefore loaded in to the software before calibration. The indexing parameters that were applied during collection are shown in Table 3.6. A screenshot from the data collection software can be seen in Figure 3.5.

Table 3.6: *Settings used in TSL OIM Data Collection 5.2*

Hough - transform	
Hough Type	Classic
Hough Resolution	Low
Binned pattern size	160 X 160
Theta Step Size	1º
Rho Fraction	0,90
Max Peak Count	8
Min Peak Count	3
Convolution Mask	Medium 9 X 9
Min Peak Magnitude	5
Min Peak Distance	15
Peak Symmetry	0,50
Vertical Bias	0 %
Hough Time	-

3.6.4 Processing and Analyzing

The software TSL OIM Analysis 6.1 was used to analyse the microstructure of the material. The two maps mainly used to analyse the microstructure was Image Quality(IQ) and Inverse Pole Figure - maps. An Inverse Pole Figure map shows the orientations of the grains by giving each grain a color according to their orientation, as explained in section 2.7.3. The Image Quality map shows the quality of each diffracted point. Phases with different amount of dislocation densities could therefore easily be separated. A Phase map, separating areas with BCC and FCC crystal structure, and a map were the image quality was averaged over each grain was also used.

The program contains different cleaning methods, the only maps cleaned in this thesis was the inverse pole figure maps, they were cleaned using a function called dilation clean up method.

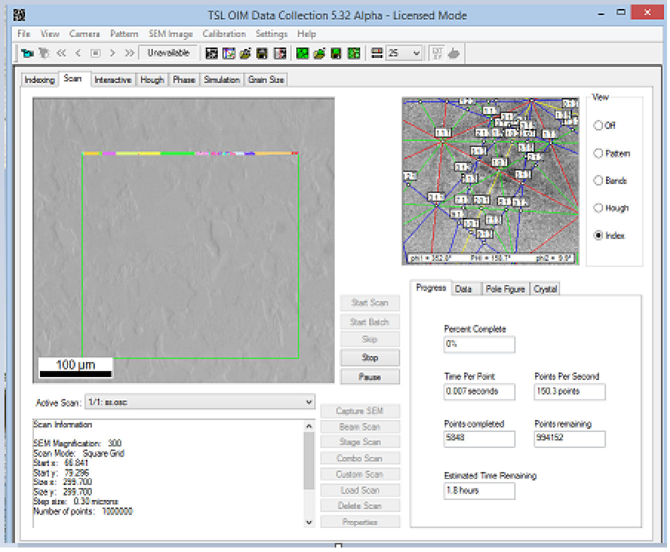

TSL OIM Data Collection 5.32 Alpha - Licensed Mode

Active Scan: 1/1: as.osc

Scan Information

SEM Magnification: 300
Scan Mode: Square Grid
Start x: 66.841
Start y: 79.296
Size x: 299.700
Size y: 299.700
Step size: 0.30 microns
Number of points: 1000000

Percent Complete: 0%
Time Per Point: 0.007 seconds
Points Per Second: 150.3 points
Points completed: 5848
Points remaining: 994152
Estimated Time Remaining: 1.8 hours

Figure 3.5: *Screenshot from the OIM TSL Data Collection software.*

3.7 Light Microscope

The light microscope used was a Leica MEF4M. Before the samples could be investigated in the microscope, they needed to be etched in 2% Nital for 12 seconds, in order to reveal the microstructure.

Chapter 4

Results

4.1 Dilatometric Analysis

Figure 4.1, 4.2 and 4.3 represent the dilatometric curves for the three steel samples cooled at different cooling rates. The red line in the figures show the temperature as a function of time, whilst the purple line show the changes in volume during heating and cooling. In Figure 4.1 the Ac1 and Ac3 temperatures are marked, these are the same for all three samples and are therefore not shown in Figure 4.2 and Figure 4.3.

The Ac1 temperature was found to be 640 °C and the Ac3 temperature was estimated to be 750 °C.

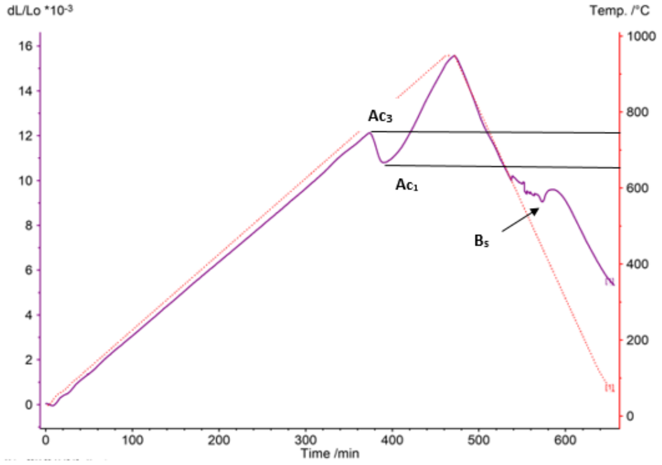

Figure 4.1: *Dilatometer curve for sample cooled at* 5 °C *per minute.*

In Figure 4.1 there are several changes in volume during cooling, one of the peaks is assumed to represent the starting of bainite formation and is marked with Bs in the figure. The other volume changes can indicate the formation of ferrite.

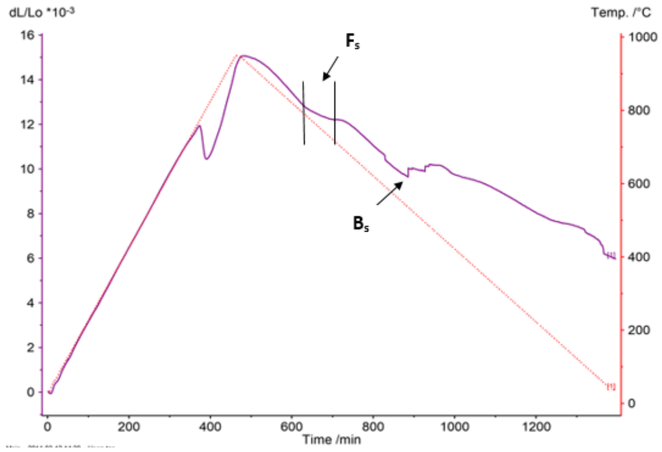

Figure 4.2: *Dilatometer curve for sample cooled at* 1 °C *per minute.*

In Figure 4.2 the dilatometer curve for the sample cooled at 1 °C per minute can be seen. In this Figure, two separate changes in volume can also be seen, where the first is assumed to be due to formation of ferrite and the second due to formation of bainite. The two volume changes are marked in the figure, where F_s indicates the start of the ferrite formation and B_s indicates the start of the bainite formation.

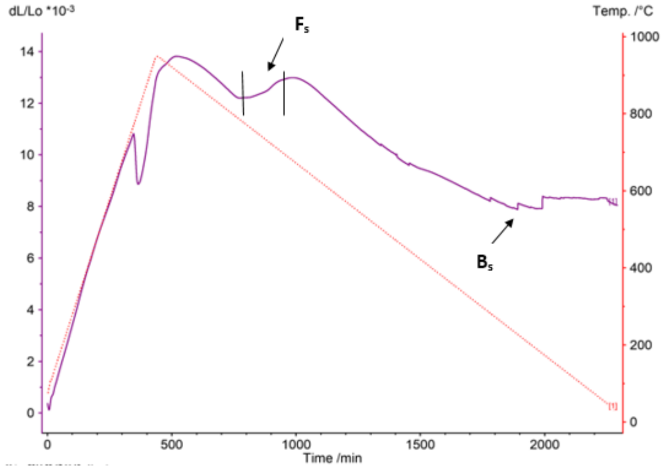

Figure 4.3: *Dilatometer curve for sample cooled at* 0, 5 °C *per minute.*

In Figure 4.3 the dilatometer curve for the sample cooled at 0, 5 °C per minute is represented. Notice that the two separate changes in volume can be seen even more clearly in this dilatometric curve than in Figure 4.2. The start of ferrite and bainite formation is marked with F_s and B_s respectively.

The bainite start temperature is approximately the same for all three samples and was found to be 550 °C.

4.2 Mechanical properties

4.2.1 Tensile Tests

Three longitudinal tensile tests were done for the base material. In Figure 4.4 a stress strain curve from one of the specimens can be seen. The tensile strength is the stress at maximum on the engineering stress-strain curve and is marked with TS in the figure. The mean tensile strength with standard deviation for the three tensile test specimens was found to be $784MPa \pm 2,36$.

The yield strength is the stress at which the material starts to deform plastically. The yield strength is marked with YS in the figure. The mean yield strength with standard deviation for the three tensile test specimens was found to be $714MPa \pm 4,50$.

From the yield and tensile strength the Yield/Tensile ratio could be calculated. The Yield/Tensile ratio was found to be 0,91.

Notice that the steel does not have a sharp yield point and that it continuous to deform plastically for quite a long time before fracture appears. The stress-strain graphs from the two other tensile test specimens can be found in Appendix F.

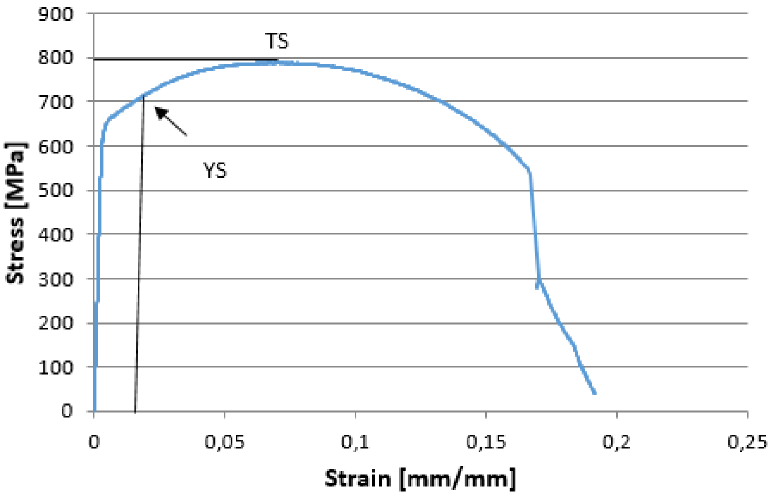

Figure 4.4: *The stress-strain curve for one of the tensile test specimens. The tensile strength is marked with TS and the yield strength is marked with YS.*

4.2.2 Vickers Hardness

The mean hardness value of the rod extracted from outer to inner diameter of the steel block was found to be $249HV5 \pm 6,18$. All the hardness values can be found in Appendix G, where it can be seen that the hardness did not show much variation through the thickness.

The mean hardness values with standard deviation for the three dilatometer samples are represented in Table 4.1. P1d is the sample cooled at 5 °C per minute, P2d the sample cooled at 1 °C per minute and P3d the sample cooled at 0, 5 °C per minute.

Table 4.1: *Mean Vickers hardness values for the three dilatometer specimens.*

	Vickers Hardness
P1d	$270HV5 \pm 6,13$
P2d	$179HV5 \pm 6,13$
P3d	$164HV5 \pm 8,81$

The sample with the lowest hardness value was the sample cooled at 0, 5 °C per minute (P3d), whilst the sample with the highest hardness value was the sample cooled at 5 °C per minute (P1d). Notice that the hardness for this sample is higher than the hardness of the base material.

4.3 Microstructure characterisation of base material

Characterisation of the microstructure of the base material was done using the EBSD technique as well as Light Microscope. More Optical micrographs and EBSD images of the base material can be found in Appendix A and Appendix B.

Figure 4.5 is a light microscope image of the base material after etching in 2% Nital. The microstructure contains very irregular grain boundaries and packets of bainite plates can clearly be seen.

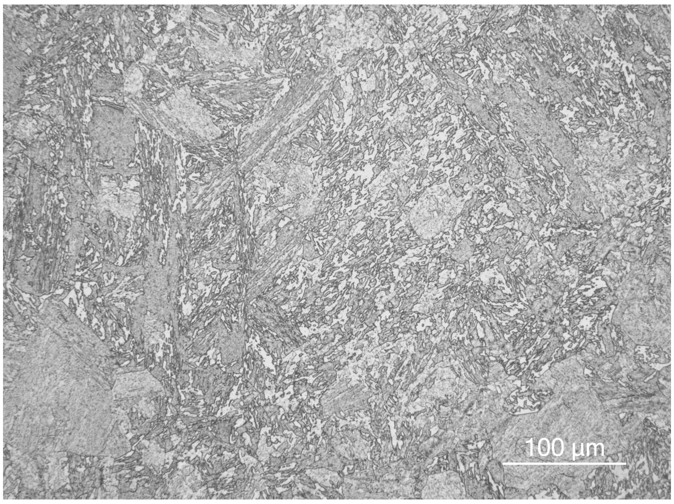

Figure 4.5: *Light Microscope image of base material etched in 2 % Nital.*

The microstructure of the base material was very difficult to image in EBSD, due to the large amount of dislocation densities in the bainite microstructure. Several attempts had to be made before a good result was obtained. In Figure 4.6 an IQ map of the base material can be seen. Most of the picture appears as dark and a bit unclear due to the low pattern quality caused by the bainitic microstructure. In Table 4.2 the average CI, IQ and Fit value for the IQ map in Figure 4.6 can be seen.

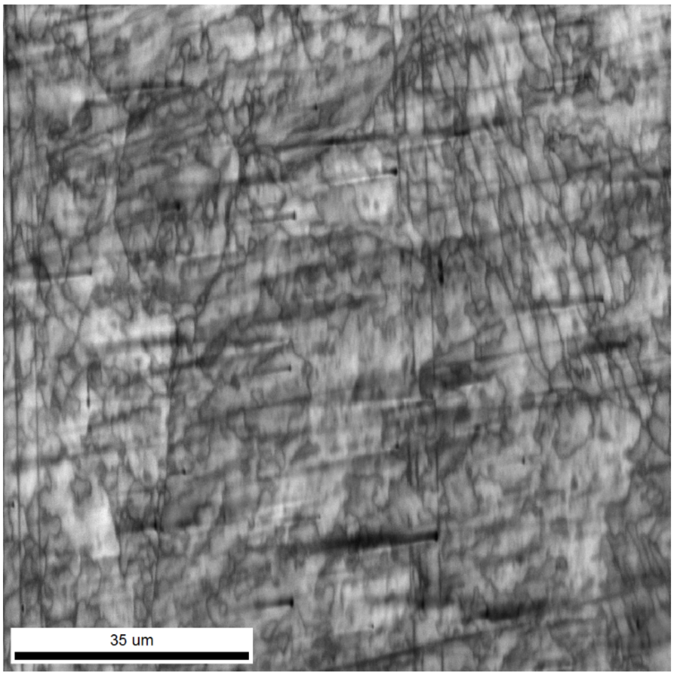

Figure 4.6: *IQ map of the base material.*

Table 4.2: *Average CI, IQ and Fit values found by the OIM TSL Analysis software for Figure 4.6.*

	Base material
CI	0,63
IQ	121,65
Fit	0,89

Figure 4.7 also represents an IQ map of the base material, but here high angle grain boundaries (>50 °) are coloured black and low angle grain boundaries (<50 °) are coloured yellow. The corresponding Table in Figure 4.7b gives the fraction of high and low angle grain boundaries. The fractions are found by the TSL OIM Analysis software.

Notice that there is a higher proportion of high angle grain boundaries than low angle grain boundaries. Some areas inside high angle grain boundaries have a high proportion of low angle grain boundaries, these areas most likely contain sub-grains.

In Figure 4.8 an inverse pole figure map of the base material can be seen. The arrow points at a former austenite grain boundary.

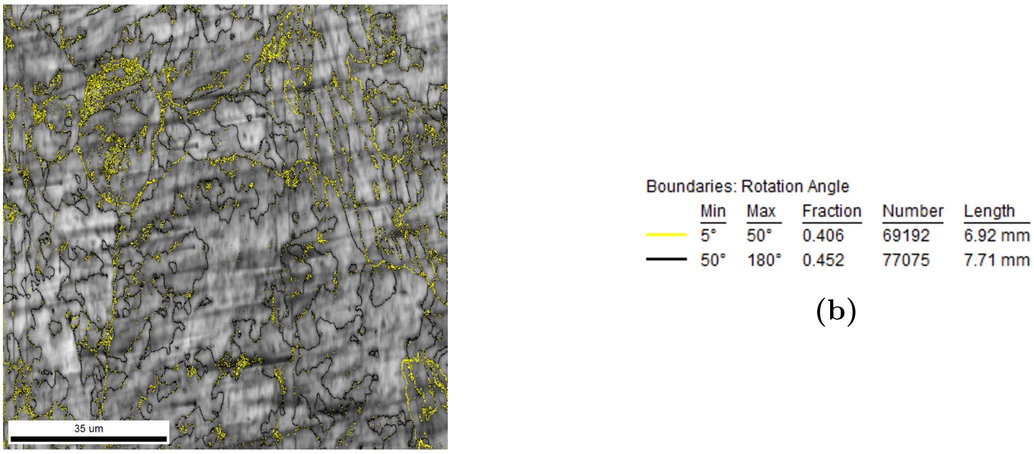

Boundaries: Rotation Angle

	Min	Max	Fraction	Number	Length
━	5°	50°	0.406	69192	6.92 mm
━	50°	180°	0.452	77075	7.71 mm

(a)

(b)

Figure 4.7: *a)IQ map of base material where high angle grain boundaries (>50°) are coloured black and low angle grain boundaries (<50°) are coloured yellow. b)Table with fraction of high and low angle grain boundaries calculated by the TSL OIM Analysis software.*

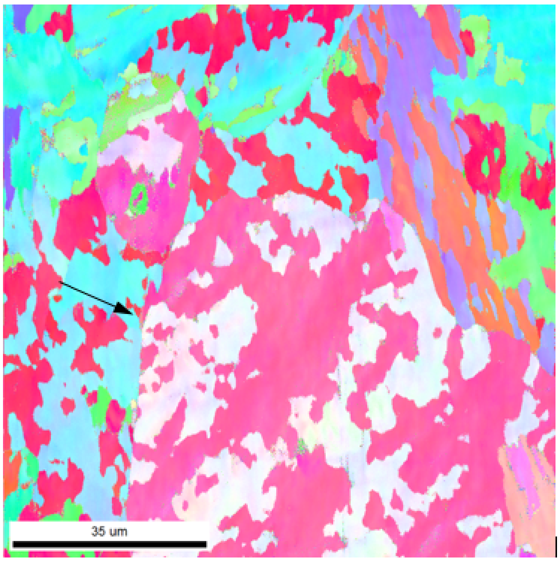

Figure 4.8: *IPF map of base material where the arrow ponits out a former austenite grain boundary.*

Figure 4.9 shows a phase map of the base material, where green and red colour represent FCC (γ)and BCC (α) structure, respectively. The fraction of the different phases, calculated by the TSL OIM Analysis software, can be seen in the table in Figure 4.9b.

In Figure 4.10 another IQ map of the base material can be seen, but here the IQ values are averaged over each grain in order to see grains with low and high IQ values, according to a chosen threshold value. Grains with an average IQ value less than 130 are coloured yellow and grains with an IQ value above 130 are coloured blue, as can be seen in the table in Figure 4.10b.

Color Coded Map Type: Phase

	Phase	Total Fraction	Partition Fraction
🟥	Iron - Alpha	0.980	0.980
🟩	Iron - Gamma	0.020	0.020

(a) **(b)**

Figure 4.9: *a) Phase map of base material where green areas represent FCC (γ) austenite and red areas represent BCC (α). b)Fraction of BCC alpha and FCC gamma phase calculated by the TSL OIM Analysis software.*

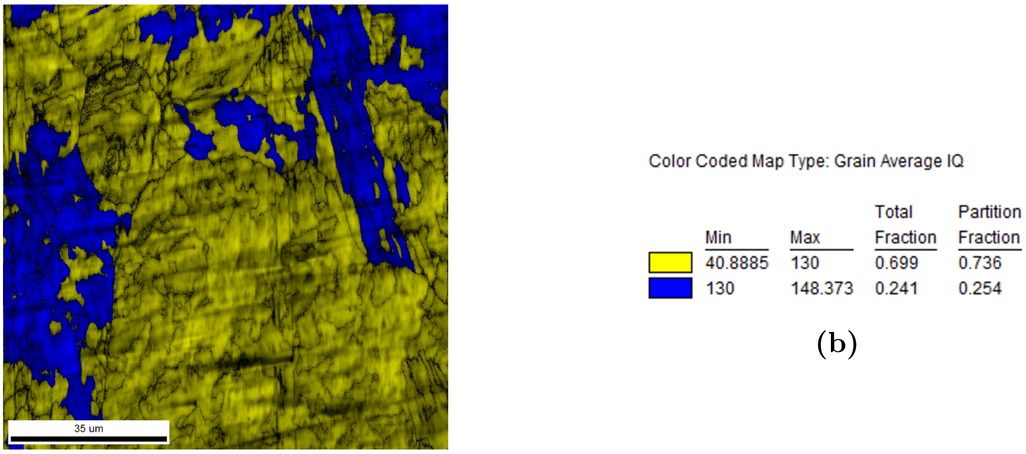

Color Coded Map Type: Grain Average IQ

	Min	Max	Total Fraction	Partition Fraction
🟨	40.8885	130	0.699	0.736
🟦	130	148.373	0.241	0.254

(a) . **(b)**

Figure 4.10: *a)IQ map of base material where the IQ value is averaged over each grain. Grains with average IQ value less than 130 are coloured yellow and grains with an average IQ value larger than 130 are coloured blue b)Fraction of IQ values higher and lower than 130 calculated by the TSL OIM Analysis software.*

4.4 Microstructure characterisation of dilatometer specimens using Light Microscope

In this section Light Microscope images of the dilatometer specimens will be presented. A magnification of 20X was used for all the pictures presented below. More images taken with the light microscope can be found in Appendix C, where different magnifications have been used.

Figure 4.11 shows the microstructure of the dilatometer sample cooled at 5 °C per minute. The microstructure consists of two different phases, where one phase exhibits white big grains, whilst the other consists of dark irregular grain boundaries with "needle" structure inside. The dark and irregular phase is almost identical to the one found in the optical micrograph of the base material, shown in Figure 4.5, and is therefore assumed to be bainite. One can clearly see that the sample contains more bainite than ferrite.

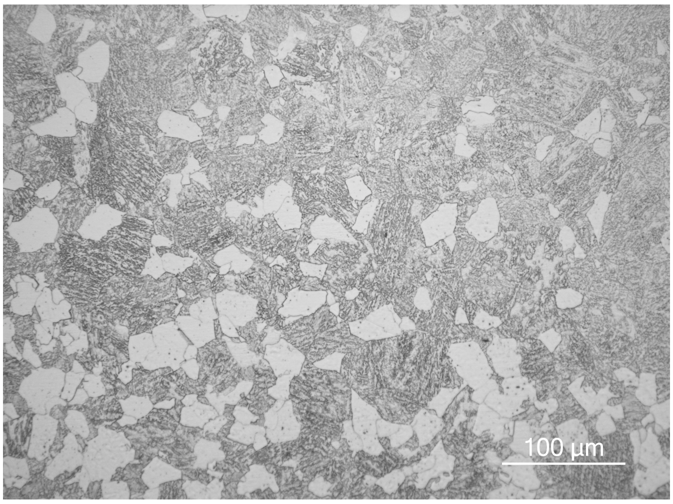

Figure 4.11: *Light Microscope image of the dilatometer sample cooled at* 5 °C *per minute and etched in 2% Nital.*

In Figure 4.12 the microstructure of the dilatometer sample cooled at 1 °C per minute can be seen. This specimen also contains a mixture of ferrite and bainite, but here the volume fraction of ferrite is larger than in the sample cooled at 5 °C per minute. Dark spots can be seen in some of the ferrite grains, these are assumed to be carbides.

Figure 4.13 represents the microstructure of the sample cooled at $0,5\,^{\circ}$C per minute. The microstructure is almost fully feritic, but with a few bainite grains

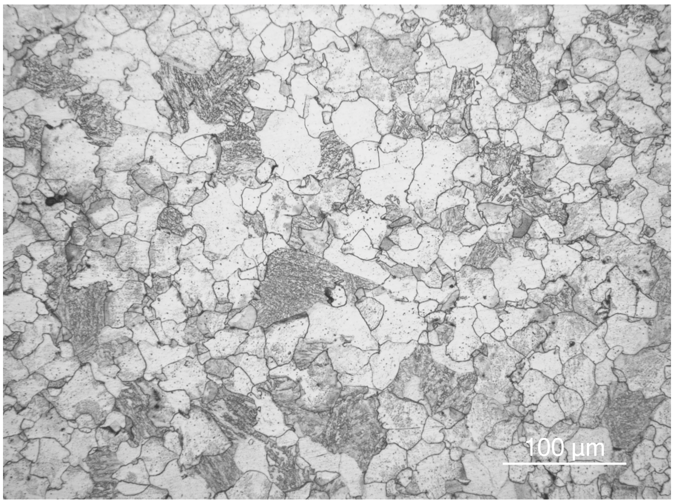

Figure 4.12: *Optical micrograph of the dilatometer sample cooled at* 1 °C *per minute and etched in 2% Nital.*

in between. In the upper left corner of the figure a few dark bainite grains can be seen. Carbides can also be seen inside the ferrite grains.

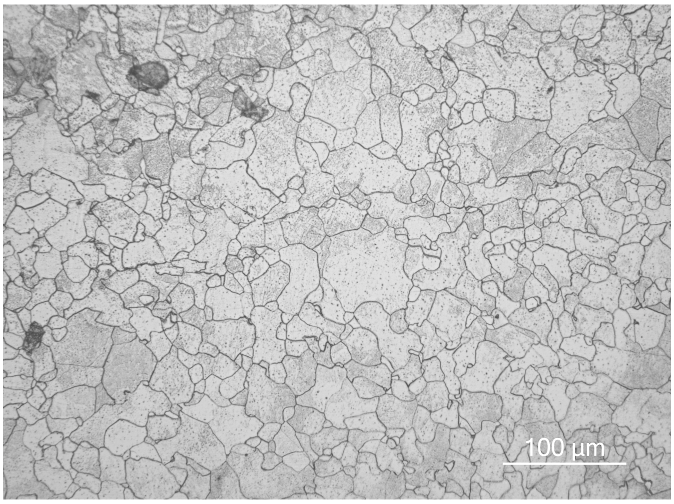

Figure 4.13: *Light Microscope image of the dilatometer sample cooled at* $0,5\,^{\circ}\mathrm{C}$ *per minute and etched in 2% Nital.*

4.5 Microstructure characterisation of dilatometer specimens using EBSD

In this section Image Quality maps and Inverse Pole figure maps of the three dilatometer specimens will be presented. More IQ and IPF maps of the samples can be found in Appendix D.

Figure 4.14 represents an IQ map of the dilatometer sample cooled at 5 °C per minute. Two different microstructures can clearly be seen, one appears as white and smooth, the other as dark and with a lot of "needles". The dark parts are assumed to be bainite, whilst the white/light parts are assumed to be ferrite. It can clearly be seen that the bainitic microstructure is the dominating one in this steel sample.

Figure 4.15 is an inverse pole figure map of the sample cooled at 5 °C per minute. The ferrite grains have a uniform colour indicating no misorientations inside. The bainite grains have an orientation variation inside the grains. In Figure 4.16 an area of the IQ map is cropped and the corresponding IPF map of the cropped area can be seen in Figure 4.16b. In the IPF map two grains are marked with F for ferrite and B for bainite. It can be seen that the ferrite grains have a uniform colour, whilst the bainite grains have an orientation variation inside.

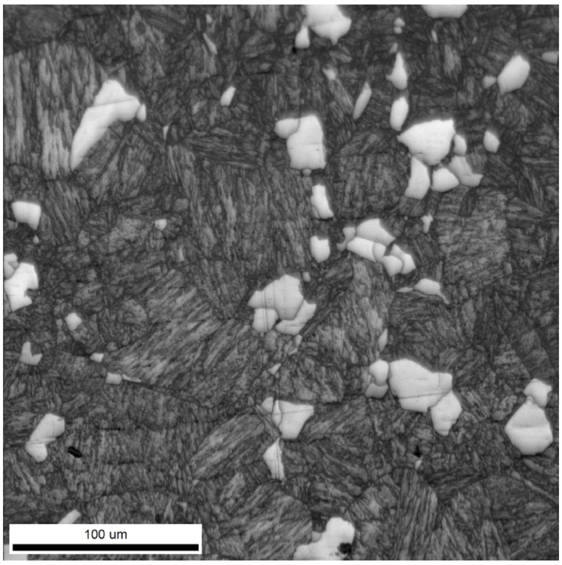

Figure 4.14: *IQ map of dilatometer sample cooled at* 5 °C *per minute.*

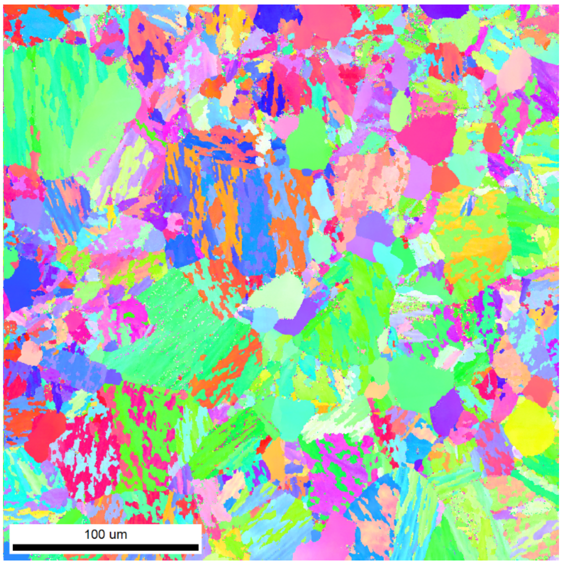

Figure 4.15: *IPF map of dilatometer sample cooled at 5 °C per minute.*

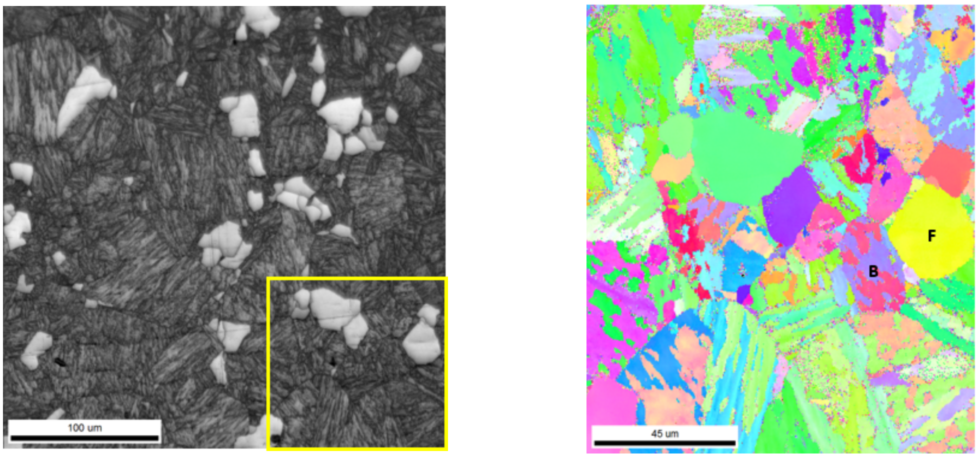

(a) **(b)**

Figure 4.16: *a)IQ map of dilatometer sample cooled at 5 °C per minute. b)Cropped IPF map of the area marked in yellow in a).*

Figure 4.17 represents the IQ map of the steel sample cooled at 1 °C. The image mostly consists of bright, smooth and quite large grains, which most likely are ferrite grains. Some dark areas can be seen, these are very similar to the dark structure in Figure 4.14 and are therefore assumed to be bainite. Notice that this steel samples contains a higher amount of ferrite than the steel sample cooled at 5 °C per minute.

The IPF map of the dilatometer sample cooled at 1 °C is shown i Figure 4.18. The ferrite grains can easily be separated from the bainite grains, considering they have a uniform colour.

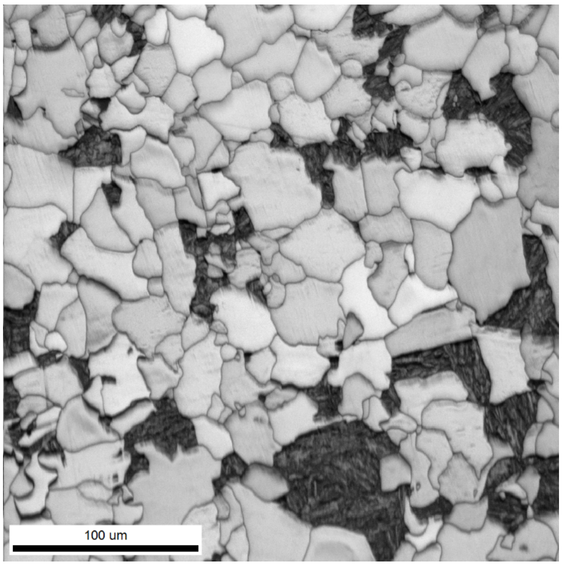

Figure 4.17: *IQ map of dilatometer sample cooled at* 1 °C *per minute.*

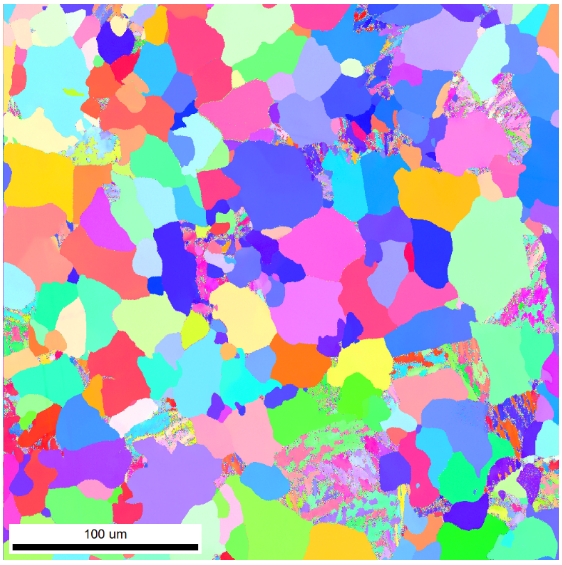

Figure 4.18: *IPF map of dilatometer sample cooled at* 1 °C *per minute.*

In Figure 4.19 the IQ map of the steel sample cooled at 0.5 °C per minute is shown. Large parts of the image consist of white large ferritic grains. Only a few bainitic grains can be seen. Abrasive stripes from the grinding or polishing can be seen. Several attempts were made in preparing the sample so that no abrasive stripes were present, however this was very difficult due to the softness of the ferritic microstructure.

Figure 4.20 is an inverse pole figure map of the sample cooled at 0.5 °C per minute. The bainite grains can easily be separated from the ferrite grains, as they have an orientation variation inside.

Notice that the dilatometer sample cooled at 0.5 °C per minute has the highest amount of ferrite of the three dilatometer specimens.

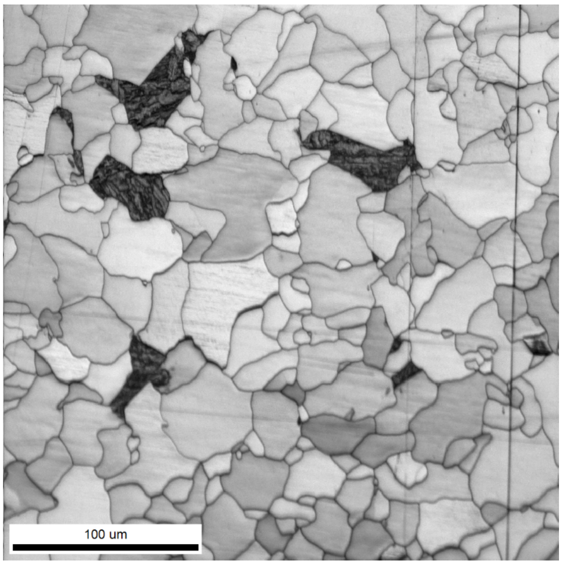

Figure 4.19: *IQ map of dilatometer sample cooled at* 0.5 °C *per minute.*

Table 4.3 represents the average CI, IQ and Fit values for Figure 4.14, 4.17 and 4.19, the values are found by the TSL OIM Analysis software. P1d is the sample cooled at 5 °C per minute, P2d the sample cooled at 1 °C per minute and P3d the sample cooled at 0.5 °C per minute. Notice that the quality of the pictures increase with decreasing cooling rate and increasing ferrite content.

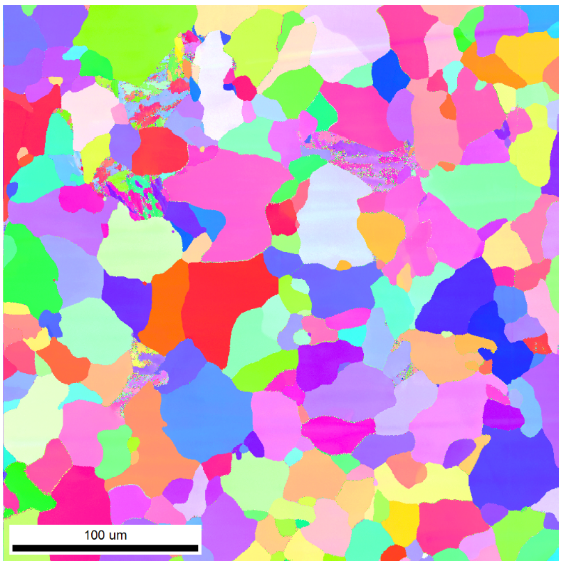

Figure 4.20: *IPF map of dilatometer sample cooled at* 0.5 °C *per minute.*

Table 4.3: *Average CI, IQ and Fit values, found by the TSL OIM Analysis software, for the IQ maps presented in this section.*

	P1d	*P2d*	*P3d*
CI	0,45	0,72	0,73
IQ	110,03	185,38	193,87
Fit	1,14	0,71	0,57

4.6 Microstructure characterisation of dilatometer specimens using BSE imaging

In this section BSE images of the three dilatometer specimens will be presented. More BSE images of the samples can be found in Appendix E.

Figure 4.21 is a BSE image of the dilatometer sample cooled at 5 °C per minute. Two different phases can be distinguished from this picture; the grains that exhibit a uniform contrast are assumed to be ferrite, whereas the grains that display a varied contrast inside are assumed to be bainite. The variation in contrast is due to the substructures inside bainite grains. The two phases are marked with F for ferrite and B for bainite respectively.

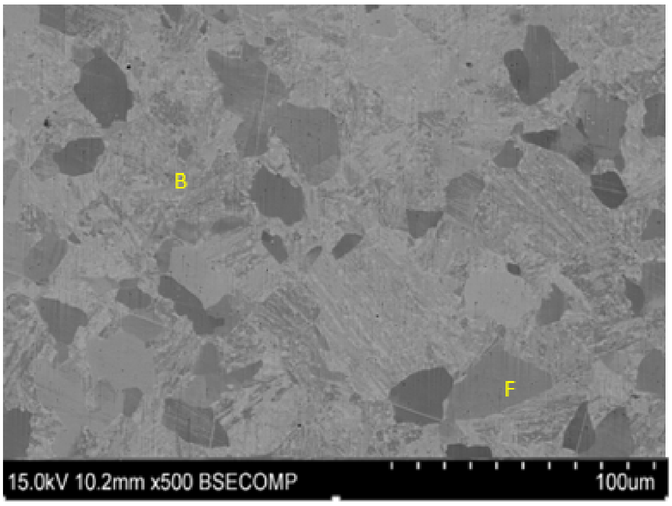

Figure 4.21: *BSE image dilatometer sample cooled at* 5 °C *per minute.*

Figure 4.22 is a bascatter electron image of the steel sample cooled at 1 °C per minute. Both ferrire and bainite grains can also be seen in this sample, but here the volume fraction of ferrite is larger than for the sample cooled at 5 °C per minute. Two areas marked with a B, for bainite and two areas marked with an F, for ferrite can be seen in the figure. Some areas of the ferrite appear as brighter than others due to different crystal orientation.

In Figure 4.23 a close up of the bainitic phase in the dilatometer specimen cooled at 1 °C per minute can be seen. In this figure it can clearly be seen that the bainite contains sub-grains.

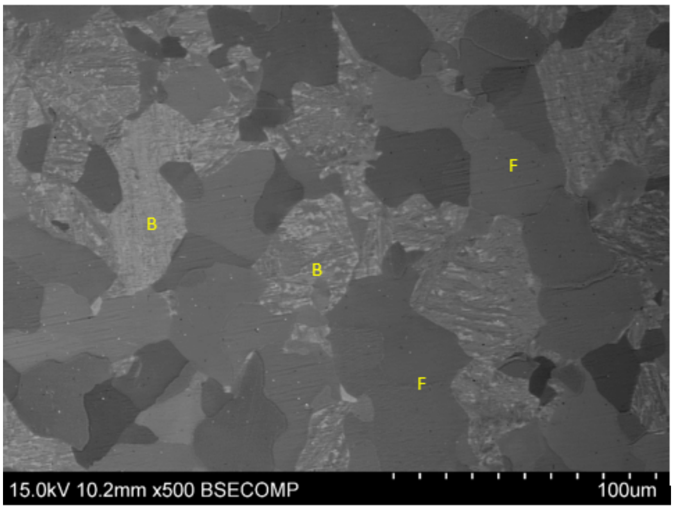

Figure 4.22: *BSE image of dilatometer sample cooled at* 1 °C *per minute.*

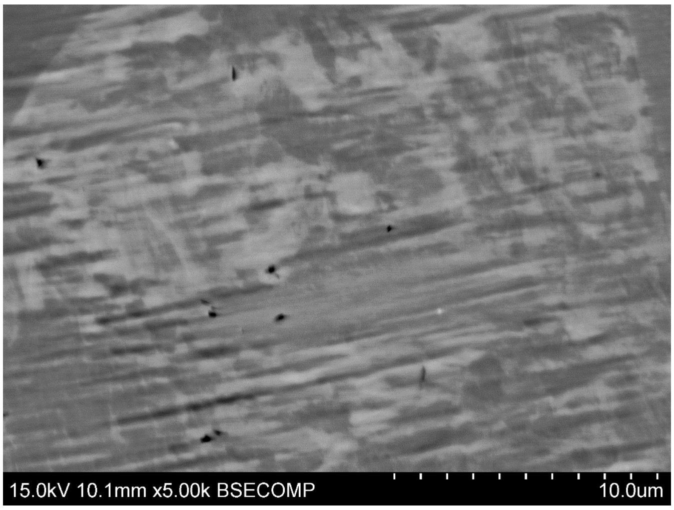

Figure 4.23: *BSE image of the bainite phase in the dilatometer sample cooled at* 1 °C *per minute.*

Figure 4.24 represents the BSE image of the sample cooled at $0,5\,^{\circ}\mathrm{C}$ per minute. As for the other BSE images one can see both ferrite and bainite grains in the image. This sample contains more ferrite than bainite, only a few bainite grains can be observed. White stripes can be seen in the picture, these are abrasive stripes from the grinding.

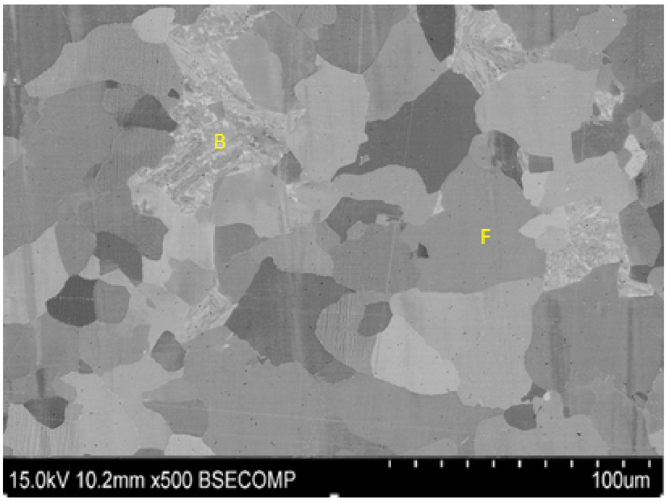

Figure 4.24: *BSE image of dilatometer sample cooled at* $0,5\,^{\circ}\mathrm{C}$ *per minute.*

4.7 Carbides in dilatometer specimens

The following figures are BSE images of particles found in the dilatometer specimens.

In Figure 4.25 two BSE images of the dilatometer sample cooled at 1 °C per minute can be seen. Figure 4.25b is a close up of the particles observed in Figure 4.25a. The particles are bright compared to the background, this indicates that they have a higher atomic number than the matrix.

Figure 4.26 represents BSE images of the dilatometer sample cooled at 0, 5 °C per minute, where Figure 4.26b is a close up of the particles seen in Figure 4.26a. Notice that a lot more particles can be observed for this sample than for the dilatometer sample cooled at 1 °C per minute.

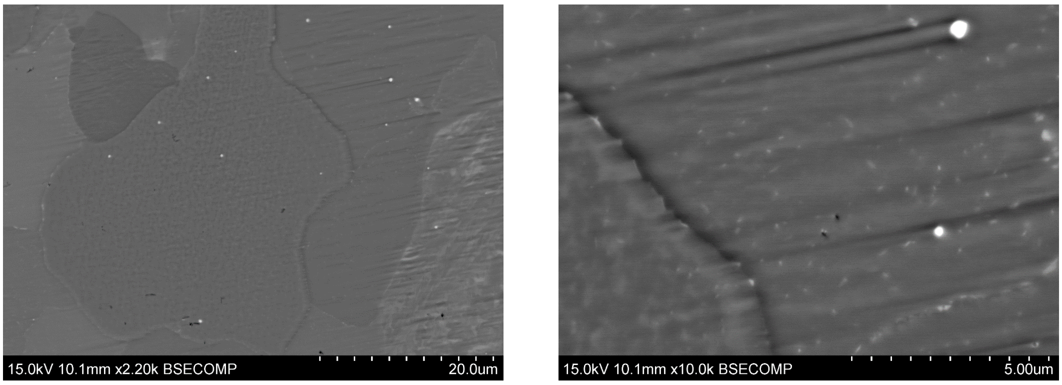

(a) **(b)**

Figure 4.25: *a)BSE image of dilatometer sample cooled at* 1 °C *per minute, where bright particles can be seen. b)Close up of particles in a).*

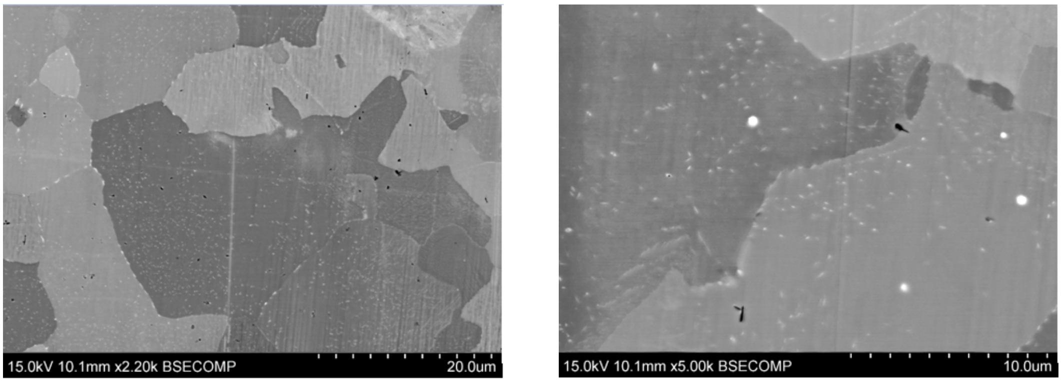

(a) **(b)**

Figure 4.26: *a)BSE image of dilatometer sample cooled at* 0,5 °C *per minute, where bright particles can be seen. b)Close up of particles in a).*

4.8 Investigation of fracture surface

One tensile test specimen was prepared for EBSD imaging in order to take a closer look at the fracture surface. In Figure 4.27 an overview of the fracture can be seen. Figure 4.28 shows a close up of the fracture surface. It can be seen that the fracture surface of the steel consists of large dimples and microvoids, these are well known characteristics of ductile fractures.

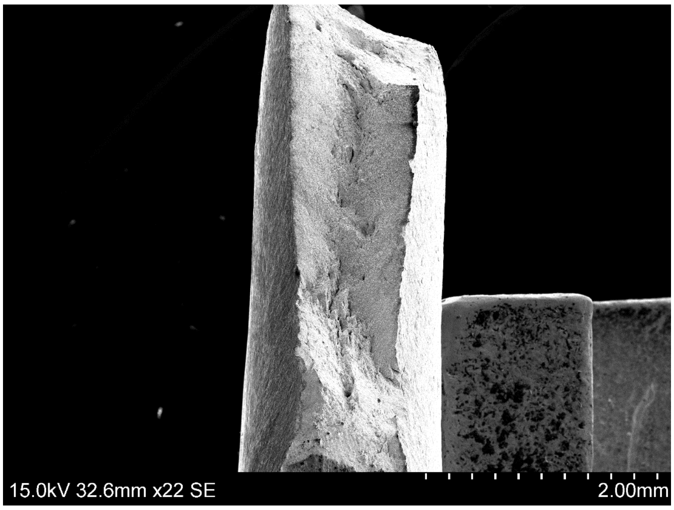

Figure 4.27: *Overview of fracture surface after tensile testing of base material.*

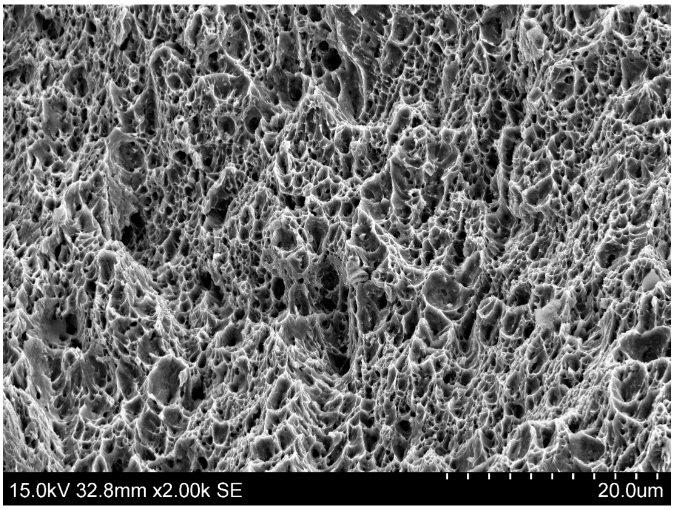

Figure 4.28: *Close up of fracture surface after tensile testing of base material.*

Chapter 5

Discussion

5.1 Microstructure characterisation of base material

An attempt was made in order to characterize the microstructure of the base material, using Light Microscope images and EBSD. Figure 4.5 represents an optical micrograph of the base material taken at 20X magnification. The microstructure contains irregular grain boundaries and packets of what looks like bainite plates. Detailed features of the microstructure was however difficult to identify from the micrograph and high magnification EBSD images were therefore studied. From Figure 4.6 an IQ map of the base material can be seen. The map appears as dark and a bit unclear due to the low pattern quality caused by high dislocation density in the microstructure. As explained in section 2.3.2 it can be difficult to characterise bainite using EBSD because the microstructure contains a large amount of dislocations, leading to poor diffraction patterns, which is evident in Figure 4.6. The low pattern quality can itself be a sign that the microstructure is fully bainitic.

In Figure 4.7 an IQ map of the base material, with high and low angle grain boundaries can be seen. The yellow lines represent low angle grain boundaries, in the range $5-50\,^{\circ}$ and the black lines represent high angle grain boundaries in the range $50-180\,^{\circ}$. Valuable information can be found from the grain boundaries, for instance information regarding sub-grains and type of bainite. Upper bainite is found to display a great number of low angle grain boundaries and few grain boundaries with an angle $>50\,^{\circ}$. Lower bainite on the other hand exhibits a high proportion of boundaries with misorientation in the range $50-60\,^{\circ}$ and few boundaries with low misorientation [29]. From the figure it can be seen that most of the grain boundaries are high angle grain boundaries, where low angle grain boundaries only appear inside the high angle grain boundaries, and gives the impression of being sub-grains. Sub-grains are a common feature in the bainitic microstructure, this discovery therefore strengthens the assumption that the steel consists of a bainitic microstructure. As a consequence of the microstructure containing more high than low angle grain boundaries it can be assumed to consist of lower bainite. However this theory needs more research to be said for sure.

Figure 4.9 is a phase map of the base material, showing areas with BCC crystal structure in red and FCC crystal structure in green. The map was constructed in order to find out whether or not the base material contained any retained austenite. As can be seen in the corresponding table in Figure 4.9b the fraction of detected FCC structure is only 0,020, it can also be seen from the phase map that only single pixels are indexed as FCC austenite. The conclusion one can draw from this is that the detected FCC structure is wrongly indexed and that the microsture of the base material therefore does not contain retained austenite.

As mentioned in section 2.3.2 the separation of bainite from ferrite and martensite have been done by other researchers, using a variety of different methods. An attempt was made in doing the same as Ryde [21], where the image quality is averaged over each grain and a threshold value for separating ferrite from bainite is chosen. Ryde [21] defined ferrite grains to have an average image quality value above 130 and bainite to have an average image quality value less than 130. The same was done for the map shown in Figure 4.10. Some parts of the map are coloured blue, which indicates an average IQ value above 130 and according to Ryde these grains are ferritic. However the IQ values can easily be tuned so that more or less areas of the map would be assigned the ferritic or bainitic phase. The maximum IQ value for the map investigated in the article was 255 and in the map in Figure 4.10, the maximum value was only 148, 373 as can be seen from the table in Figure 4.10b. This may indicate that the IQ values should have been tuned differently for the sample studied in this thesis. Another factor that will affect the IQ values are sample preparation and settings during EBSD scanning. The conclusion one can draw from this is that the method can not give definitive answers on what microstructure the steel contains, it depends too much on additional factors as sample preparation, contamination and choice of threshold values.

The chemical composition of the steel, shown in Table 3.1 is supposed to be an optimum combination of alloying elements to obtain the desired bainitic microstructure. Among the alloying elements molybdenum and chromium produce a separation of the bainite "nose" from that of ferrite. Carbide stabilizing additions, such as vanadium, boron, manganese and nickel retards the polygonal ferrite formation and therefore improves the bainitic hardenability [30]. Considering the optimal chemical composition it is very likely that the base material is fully bainitic.

There is a possibility that the base material could contain martensite as this microstructure also gives low pattern quality's, due to large amounts of dislocations in the microstructure. This is nevertheless unlikely considering the relatively low Vickers hardness value found for the base material and the great ductility of the steel, discussed in the next section. Nevertheless it would be interesting to investigate the steel from a section close to the surface (here only the midsection is investigated), as the possibility of formation of martensite would be greater here due to faster cooling rate.

Considering the information found from the IQ map, the IQ map with grain boundaries and the phase map, as well as the chemical composition it is safe to assume that the microstructure of the base material most likely is bainite.

5.2 Mechanical Properties of base material

The mechanical properties of the base material were tested to determine whether or not they corresponded well with the assumed microstructure. Three longitudinal tensile tests were done, ideally tensile tests would have been done in the transverse direction as well, but the lack of enough base material for specimens of the required size made it impossible. In Figure 4.4 the stress strain curve from one of the tensile specimens can be seen, where tensile strength and yield strength are marked in the graph. It can clearly be seen that the material does not have a sharp yield point, this corresponds well with the assumed bainitic microstructure, as sharp yield points are not observed in stress-strain curves of bainite [3]. The three tensile test specimens showed little variation in tensile and yield strength which indicates a homogeneous microstructure.

The mean tensile strength for the three tensile test specimens was found to be $784MPa \pm 2,36$ and the mean yield strength was found to be $714MPa \pm 4,50$. This corresponds to a yield/tensile ratio of 0,91. The high yield to tensile ratio can be a problem due to the risk of fracture shortly after plastic deformation is introduced. A lower yield to tensile ratio would ensure that there is substantial plastic deformation prior to ductile fracture. According to NORSOK M-001 [1] it is desirable in carbon and low alloy steels to have a yield to tensile ratio which does not exceed 0,90. The value found for this steel is as mentioned 0,91, however the yield and tensile strengths have a standard deviation of $\pm 4,50$ and $\pm 2,36$, respectively. The values are on the borderline of what is allowed, but several tensile test measurements should be taken, particularly in the transverse direction, as this direction was not tested in this thesis.

Notice that the steel continuous to deform plastically for quite a long time before fracture appears, as can be seen in Figure 4.4, this suggests that the material is very ductile. The ductile fracture is common for low-carbon bainitic microstructures [3]. A more thorough examination of the fracture was done by looking at the fracture surface in SEM. In Figure 4.27 an overview of the fracture surface can be seen and in Figure 4.28 a close up of the fracture taken at 2000X magnification can be seen. The fracture surface clearly consists of large dimples and microvoids, which are known characteristics of ductile fractures. This also underpins the assumption that the microstructure does not contain martensite, as it would have had a brittle fracture.

Vickers hardness (5kg) was also tested for the base material. A rod was extracted from the steel block, representing the whole thickness of the block, so that a difference in hardness through the thickness would be detected. The mean hardness value was found to be $249HV5 \pm 6,18$ and the hardness values did not vary significantly through the thickness, this suggests a homogeneous microstructure and good hardenability.

5.3 Microstructure characterisation of dilatometer specimens

Three steel samples were heated in a dilatometer with a heating rate of 2 °C per minute. They were cooled at different cooling rates in order to examine the microstructures formed in the different samples. The fastest cooling rate possible for the dilatometer was 5 °C per minute. One sample was therefore cooled at 5 °C per minute, one at 1 °C per minute and one at $0,5$ °C per minute.

Light Microscopy images, BSE images and EBSD images of the three dilatometer specimens were taken in order to investigate the microstructure. Vickers hardness values were also found to see if the hardness matched the assumed microstructure.

Figure 4.11 shows an optical micrograph of the dilatometer sample cooled at 5 °C per minute. The microstructure clearly consists of two different phases, where one phase exhibit white big grains, whilst the other consists of dark irregular grain boundaries and what appears as packets of laths. The dark and irregular phase is similar to the phase found in the base material, seen in Figure 4.5. It is therefore safe to say that the dark phase most likely consists of bainite. The white grains are ferrite. As for the base material, detailed features of the microstructure were difficult to detect from the optical micrograph's. More details of the microstructure could be seen in the BSE and EBSD images.

A BSE image of the dilatometer sample cooled at 5 °C per minute can be seen in Figure 4.21. The reason for the different intensity of the grains in the image, is the atomic number contrast. It is evident that the microstructure consists of two different phases, as detected in the optical micrograph. Some of the grains exhibit a uniform contrast and other grains display a varied contrast inside. The uniform grains are assumed to be ferritic and are marked with an F in the figure, the grains containing a varied contrast are assumed to be bainite. The variation in contrast can be due to the substructure inside bainite grains. A close up of the bainitic phase in the dilatometer sample cooled at 1 °C per minute can be seen in Figure 4.23, where small subgrains can be detected. Some of the ferrite grains appear brighter than others, this is due to different crystal orientation.

The IQ map of the dilatometer sample cooled at 5 °C per minute can be seen in Figure 4.14. It can be observed that the IQ map mainly consists of dark areas, indicating a low image quality, with a microstructure containing packets of laths. The low image quality indicates a microstructure with high dislocation density. A few very bright grains with no sub-structure inside can also be seen in the figure, these areas have a high image quality and should correspond to ferrite. In Figure 4.16b a cropped area of the IQ map can be seen in the form of an IPF map. Ferrite and bainite grains can be distinguished rather easily by looking at the cropped IPF map. The ferrite grains are the ones with a uniform colour indicating no misorientations inside, the bainite grains contain misorientations and therefore display a variation in colour within each grain.

Furthermore the mean Vickers hardness value for the dilatometer sample cooled at 5 °C per minute was found to be $270HV5 \pm 6,13$, the value can be seen in Table 4.1. Recall that the mean Vickers hardness value for the base material was found to be $249HV5 \pm 6,18$. Basically one would expect that the base material would have had a grater hardness than the dilatometer specimen, because of the ferrite found in the dilatometer specimen. Ferrite is as explained in section 2.4 a relatively soft microstructure, especially when the grain size is large. The reason for the larger hardness of the dilatometer specimen can be due to the effect of the carbides observed in Figure 4.25 and 4.26. The BSE images are of the dilatometer specimens cooled at 1 °C and 0,5 °C per minute , but a few carbides were also observed for the dilatometer sample cooled at 5 °C per minute, this can be seen in Appendix E. At slow cooling rates the carbides have time to nucleate and grow and can therefore have contributed to the higher hardness of the dilatometer sample cooled at 5 °C per minute. However this interesting finding should be investigated more thoroughly. It is worth mentioning that the Vickers hardness of the dilatometer specimens cooled at 1 °C and 0, 5 °C per minute were found to be lower than the base material, due to the high fraction of ferrite formed. This will be discussed further in the next sections.

The light microscope image of the dilatometer sample cooled at 1 °C per minute is shown in Figure 4.12, naturally it contains more ferrite than the dilatometer sample cooled at 5 °C per minute. The dark phase is very similar to the one found for the faster cooled sample, it is therefore safe to assume that the phase is bainite. In Figure 4.13 the microstructure of the dilatometer sample cooled at 0, 5 °C per minute can be seen. As expected this sample contains even more ferrite than the dilatometer sample cooled at 1 °C per minute. Only a few bainite grains can be observed in the upper left corner of the figure. Notice the dark spots inside the ferrite grains for both of the dilatometer specimens. These are carbides and will be further discussed in relation to the BSE images.

In Figure 4.22 and 4.24 BSE images of the dilatometer samples cooled at 1 °C and 0, 5 °C per minute can be seen. Just as for the light microscope images of the two samples, both ferrite and bainite can be observed in the microstructure. A larger amount of ferrite can be observed in the sample cooled at 0, 5 °C per minute than in the one cooled at 1 °C per minute, as expected. Small details of the microstructure could not be detected using BSE, therefore EBSD was used to investigate the microstructure further.

In Figure 4.17 and 4.19 the IQ maps of the samples cooled at 1 °C and 0, 5 °C per minute can be seen. It can clearly be observed that both of the samples contain a rather large amount of ferrite grains. The two different phases can easily be separated and both of the maps have high IQ and CI values, represented in Table 4.3. The phase that appear as dark is similar in all of the dilatometer specimens, it is therefore safe to assume that the samples contain the same phase, and that the dark phase most likely is bainite.

The Vickers hardness values for the dilatometer samples cooled at 1 °C and 0, 5 °C per minute was also measured. The values are expressed in Table 4.1 and was found to be $179HV5 \pm 6,13$ and $164HV5 \pm 8,81$ respectively. As expected the hardness values decrease with increasing amount of ferrite in the samples.

An interesting finding was that the diffraction patterns of the dilatometer samples were much easier to index than the ones for the base material, even though they contained bainite as well. The reason for this can be the large amount of ferrite formed, especially in the dilatometer samples cooled at 1 °C and 0, 5 °C per minute. As explained before ferrite is much easier to index than bainite, due to less dislocation densities. It can also be a possibility that the slow cooling has led to fewer dislocation densities in the bainite structure.

5.3.1 Carbides in dilatometer specimens

In Figure 4.25 and 4.26 BSE images of carbides observed in the dilatometer samples cooled at $1\,^{\circ}\mathrm{C}$ and $0,5\,^{\circ}\mathrm{C}$ per minute can be seen. The particles are bright compared to the background, which means that they have a higher atomic number than the matrix. It was attempted to identify the particles by EDS, but they were too small too be detected. However the chemical composition of the steel contains different alloying elements and 0,25 % carbon, as can be seen in Table 3.1. It can therefore be assumed that the carbides can consist of iron, chromium, molybdenum or niobium. The fraction of carbides also increases with increasing amount of carbon [11]. The amount of carbides increased with decreasing cooling rates, this is natural as slower cooling will lead to more nucleation and growth of particles.

Chapter 6

Conclusion

In this master thesis the microstructure and mechanical properties in the midsection of a high strength low alloy bainitic steel has been investigated. Light microscopy, backscatter electron microscopy and EBSD have been used to characterise the microstructure. The mechanical properties were tested by measuring Vickers hardness (5kg) as well as tensile and yield strengths. Three steel samples were also heated in a dilatometer and cooled at different cooling rates in order to investigate the different microstructures formed. The work can be concluded as follows.

The experiments have proven that the microstructure of the base material most likely consists of a homogeneous bainitic phase. This was proven both by the investigation of the microstructure and by the good mechanical properties found. The homogeneous microstructure and mechanical properties also indicate good hardenability.

Investigation of the dilatometer specimens showed formation of ferrite for all cooling rates used in this thesis, as well as a reduction in Vickers hardness with decreasing cooling rates and increasing ferrite content. The conclusion that can be drawn from this is that the cooling in the midsection of the steel can not be 5 °C per minute or slower, if a homogeneous bainitic microstructure is to be achieved.

Nucleation and growth of carbides were detected in the dilatometer specimens. Especially the ones cooled at 1 °C and 0, 5 °C per minute. The carbides proved to be heavier than the matrix and increased in number with slower cooling rates.

Chapter 7

Further Work

To get a better understanding of the microstructure and mechanical properties of the HSLA bainitic steel investigated in this thesis, the following work should be performed:

- An investigation of the microstructure and properties from other sections of the steel would be useful, in order to see if the microstructure and properties are different at the surface.
- The reason for the higher Vickers hardness in the dilatometer sample cooled at 5 °C per minute should be investigated more thoroughly.
- It would be useful to investigate the microstructure formed in the steel at faster cooling rates than 5 °C per minute, to see at what cooling rate a fully bainitic steel is achieved.
- A further investigation of what type of bainite the steel consists of would be beneficial.
- Tensile tests in transversal direction should be done as well as further investigation of mechanical properties.

Appendix A

Light Microscope images of base material

The figures below represent optical micrographs (OM) of the base material, taken with different magnifications. Figure A.1 and A.2 are taken with 10X magnification. Figure A.3, A.4 and A.5 are taken with 50X magnification. Figure A.6, A.7 and A.8 are taken with 100X magnification.

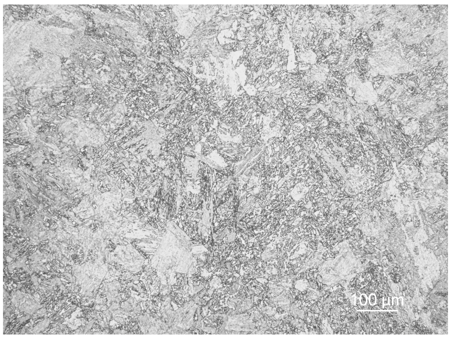

Figure A.1: *OM of base material.*

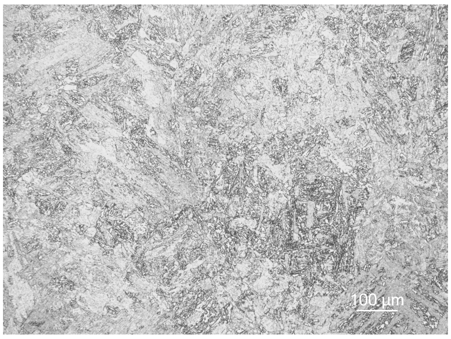

Figure A.2: *OM of base material.*

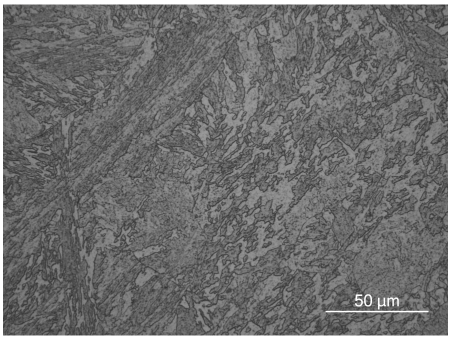

Figure A.3: *OM of base material.*

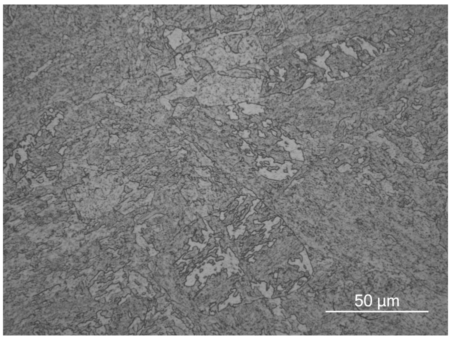

Figure A.4: *OM of base material.*

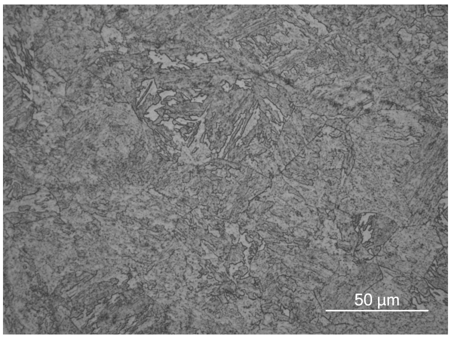

Figure A.5: *OM of base material.*

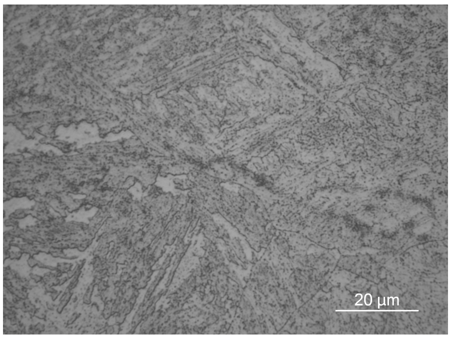

Figure A.6: *OM of base material.*

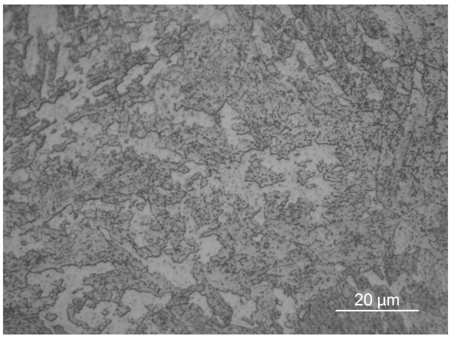

Figure A.7: *OM of base material.*

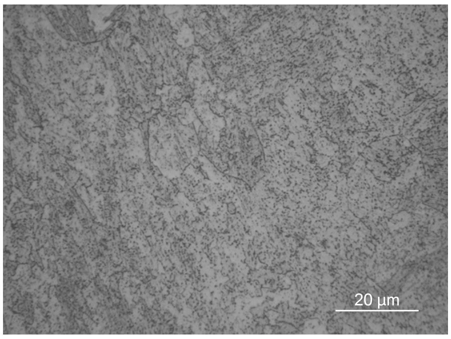

Figure A.8: *OM of base material.*

Appendix B

EBSD images of base material

The figures below represent IQ maps and IPF maps of the base material. More scans were done, but all have very bad quality and were therefore decided not to be shown here.

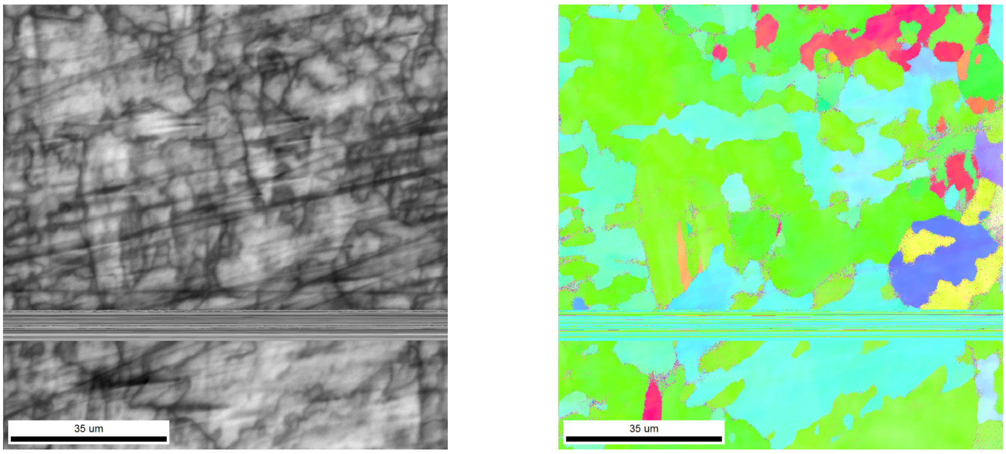

(a) **(b)**

Figure B.1: *a)IQ map of base material b)IPF map of base material.*

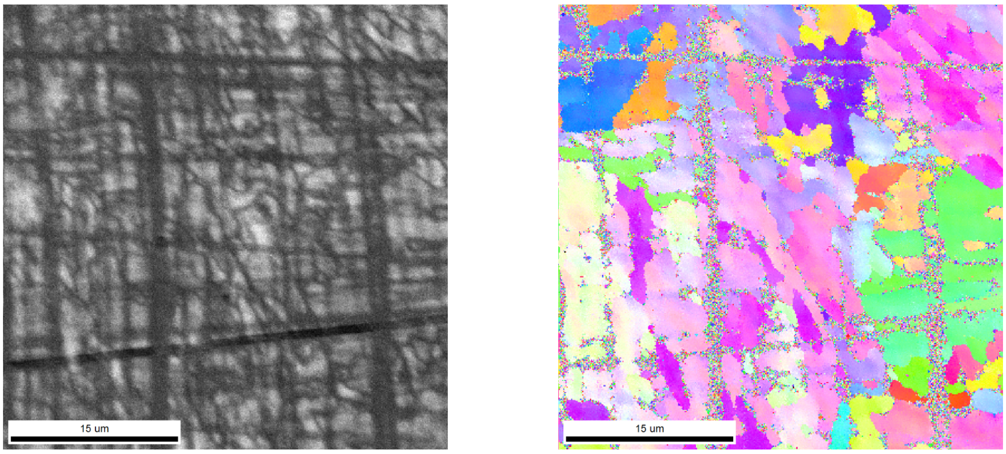

(a) (b)

Figure B.2: *a)IQ map of base material b)IPF map of base material.*

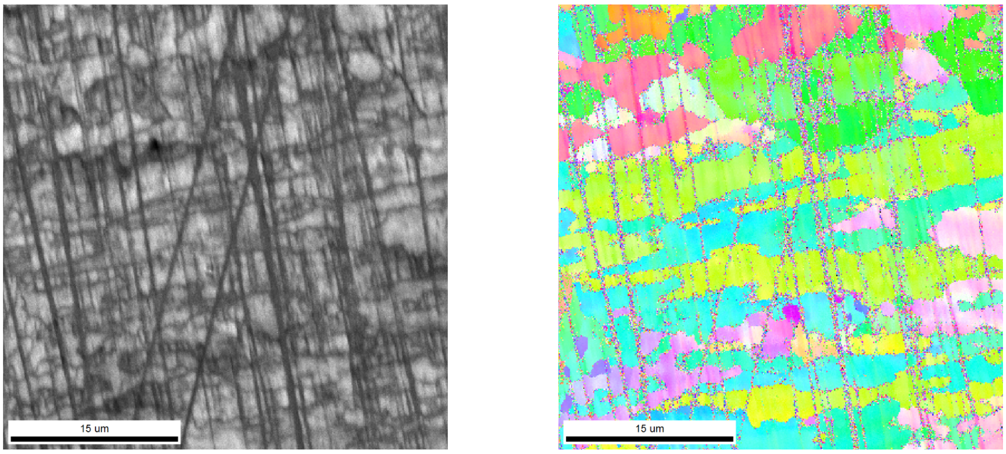

(a) (b)

Figure B.3: *a)IQ map of base material b)IPF map of base material.*

Appendix C

Light Microscope Images of dilatometer specimens

C.1 P1d

Figure C.1 to C.8 represent optical micrographs (OM) of the dilatometer sample cooled at 5 °C per minute. The sample is called P1d in the following figures.

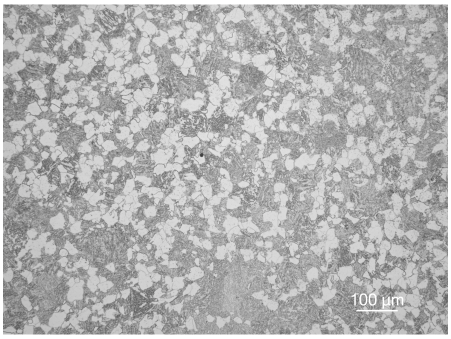

Figure C.1: *OM of P1d at 10X mag.*

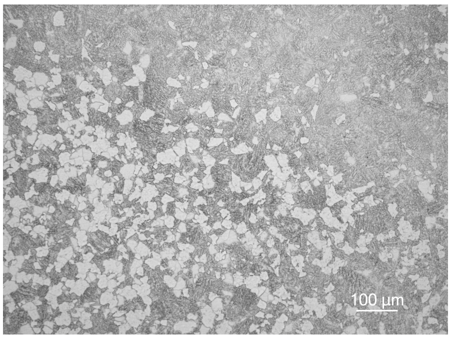

Figure C.2: *OM of P1d at 10X mag.*

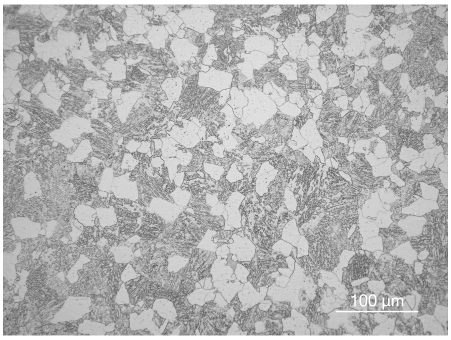

Figure C.3: *OM of p1d at 20X mag.*

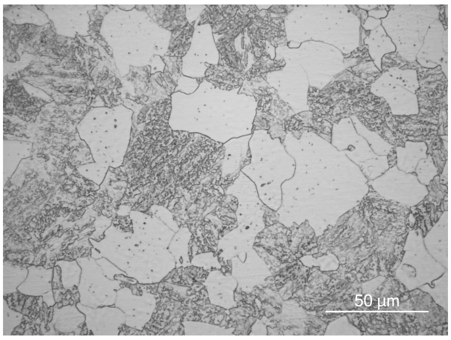

Figure C.4: *OM of P1d at 50X mag.*

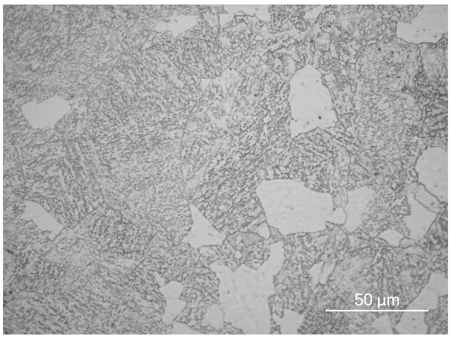

Figure C.5: *OM of P1d at 50X mag.*

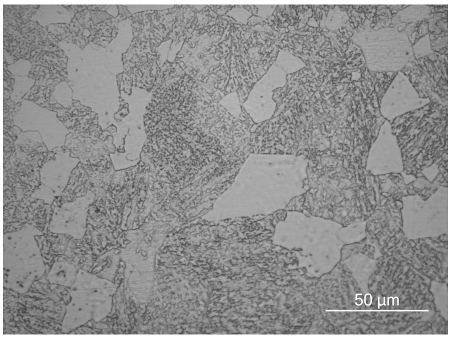

Figure C.6: *OM of P1d at 50X mag.*

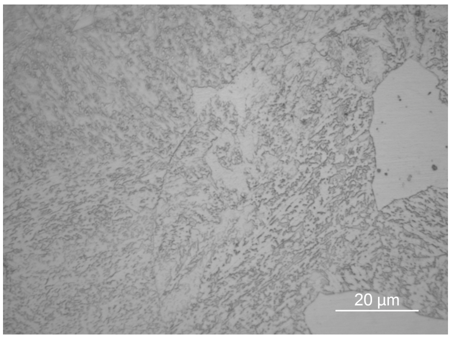

Figure C.7: *OM of P1d at 100X mag.*

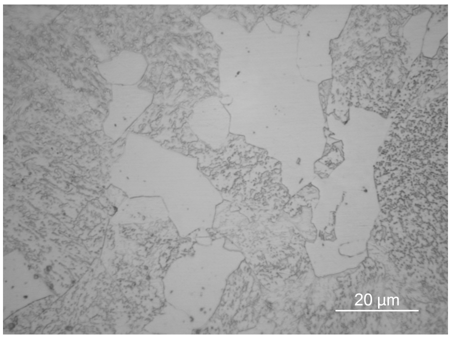

Figure C.8: *OM of P1d at 100X mag.*

C.2 P2d

Figure C.9 to Figure C.16 represent optical micrographs (OM) with different magnification of the dilatometer sample cooled at 1 °C per minute. The sample is called P2d in the figures below.

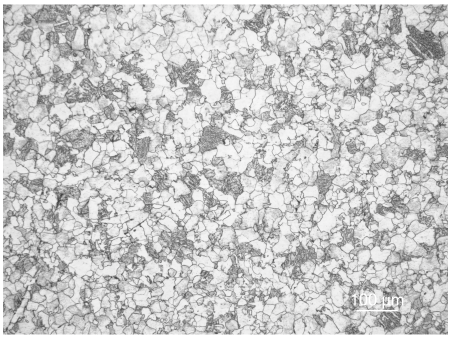

Figure C.9: *OM of P2d at 10X mag.*

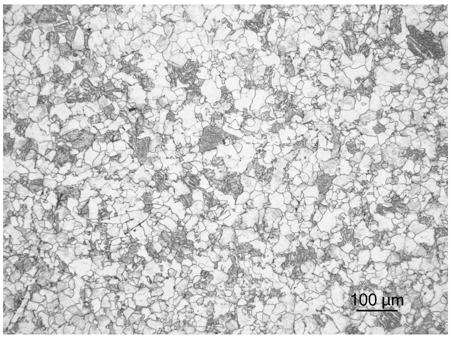

Figure C.10: *OM of P2d at 10X mag.*

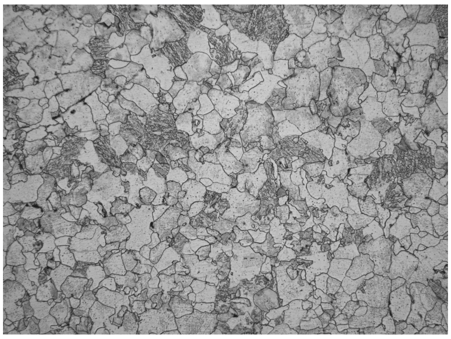

Figure C.11: *OM of P2d at 20X mag.*

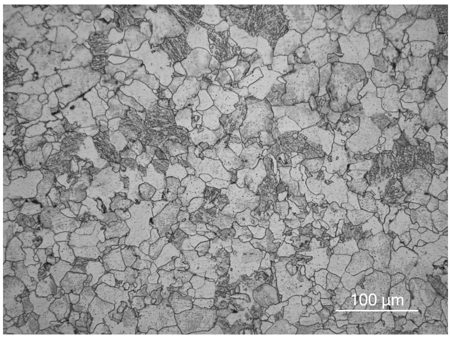

Figure C.12: *OM of P2d at 20X mag.*

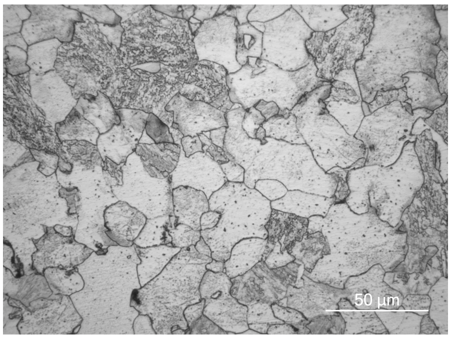

Figure C.13: *OM of P2d at 50X mag.*

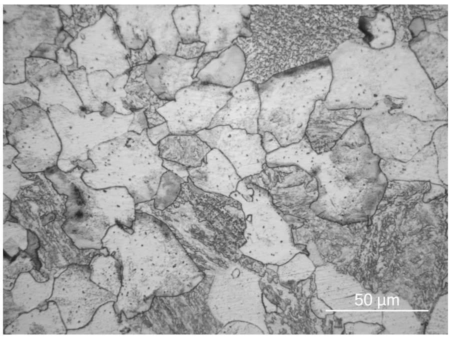

Figure C.14: *OM of P2d at 50X mag.*

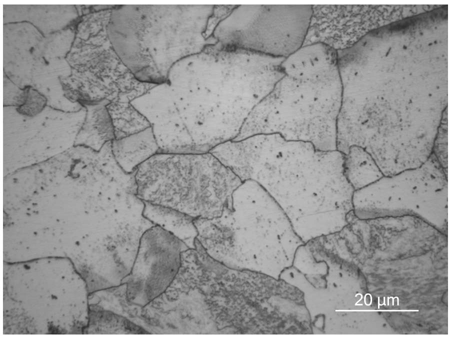

Figure C.15: *OM of P2d at 100X mag.*

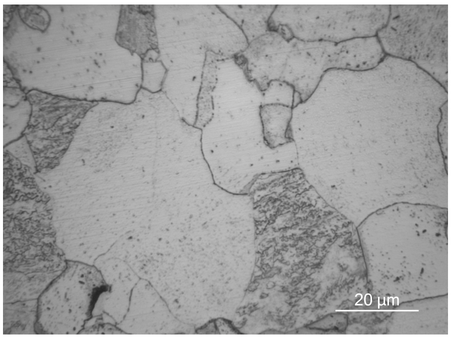

Figure C.16: *OM of P2d at 100X mag.*

C.3 P3d

Figure C.17 ti Figure C.22 represent optical micrographs(OM) with different magnifications of the dilatometer sample cooled at 0, 5 °C per minute. The sample is called P3d in the figures below.

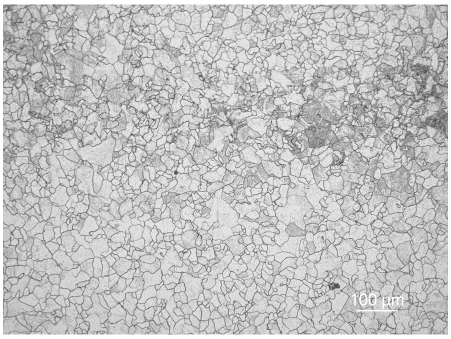

Figure C.17: *OM of P3d at 10X mag.*

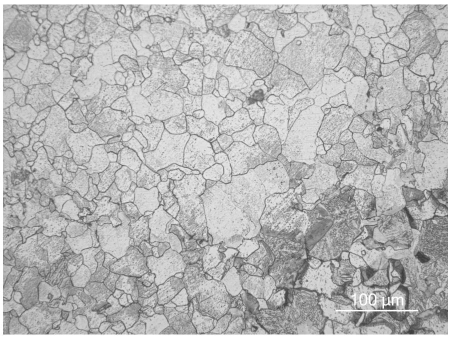

Figure C.18: *OM of P3d at 20X mag.*

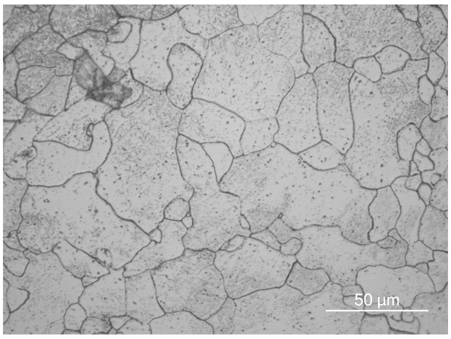

Figure C.19: *OM of P3d at 50X mag.*

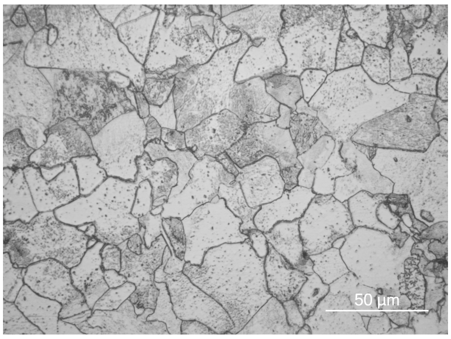

Figure C.20: *OM of P3d at 50X mag.*

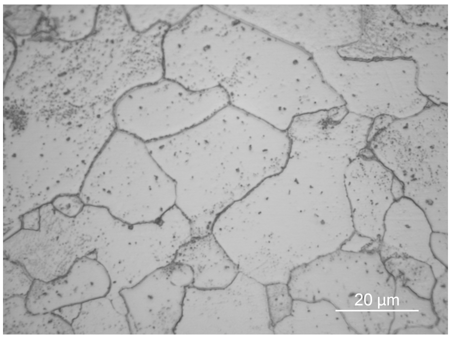

Figure C.21: *OM of P3d at 100X mag.*

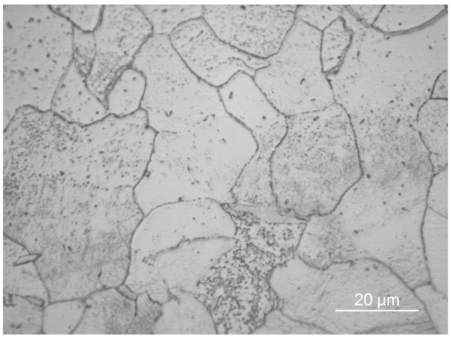

Figure C.22: *OM of P3d at 100X mag.*

Appendix D

EBSD images of dilatometer specimens

In the figures below IQ maps and IPF maps of the dilatometer specimens cooled at 5 °C, 1 °C and 0, 5 °C per minute can be seen. During some of the scans the camera got hot, therefore only half of the scan can be seen in Figure D.2. More scans were done, but only the ones with the best quality was chosen to be shown here.

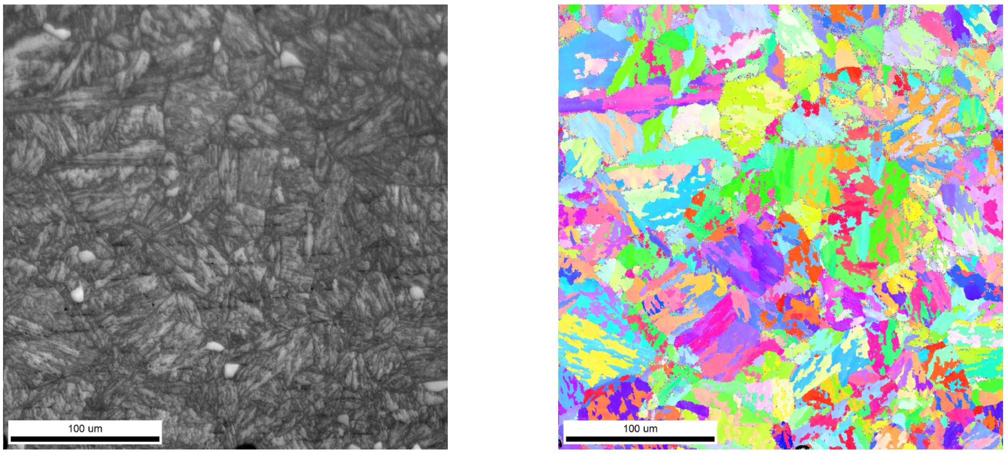

(a) **(b)**

Figure D.1: *a)IQ map of dilatometer sample cooled at* 5 °C *per minute b)IPF map of dilatometer sample cooled at* 5 °C *per minute.*

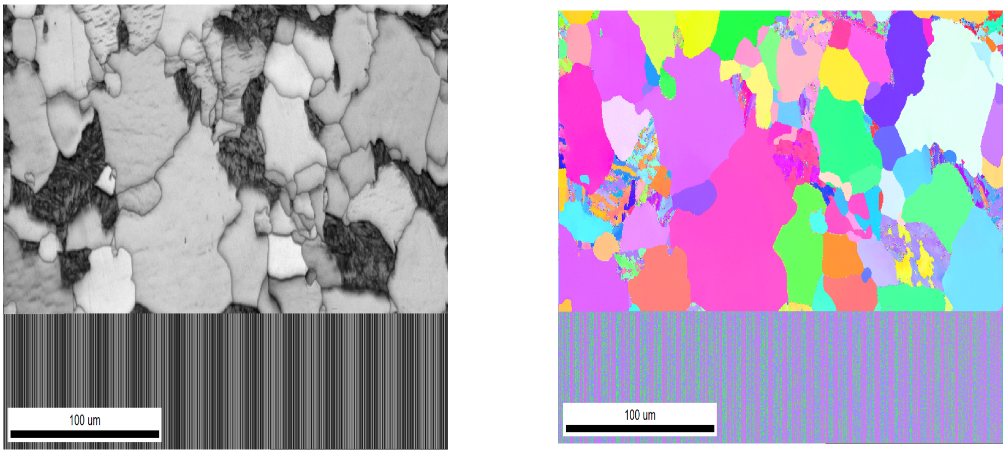

(a) **(b)**

Figure D.2: *a)IQ map of dilatometer sample cooled at* 1 °C *per minute b)IPF map of dilatometer sample cooled at* 1 °C *per minute.*

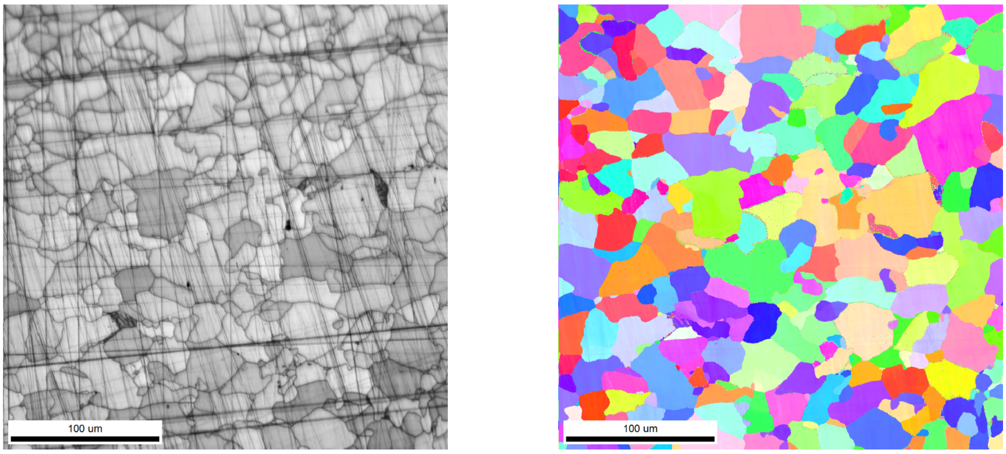

(a) **(b)**

Figure D.3: *a)IQ map of dilatometer sample cooled at* 0, 5 °C *per minute, where a lot of abrasive stripes can be seen b)IPF map of dilatometer sample cooled at* 0, 5 °C *per minute.*

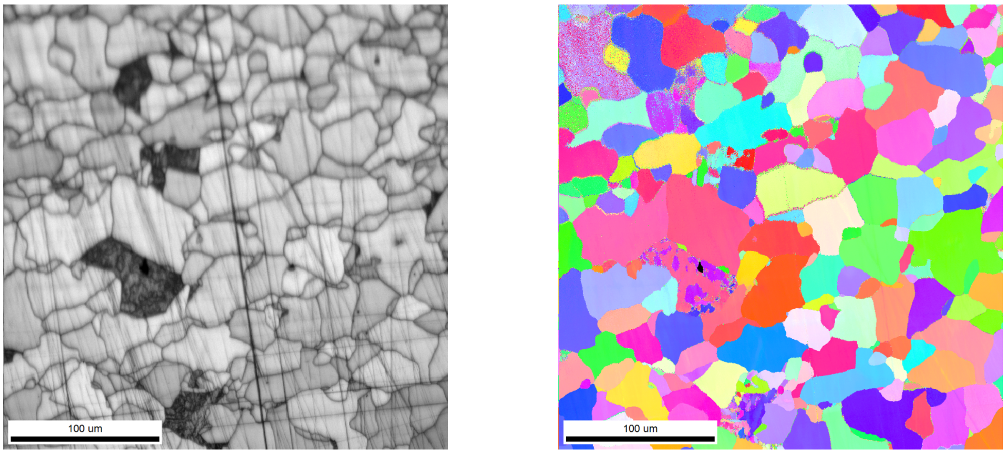

(a) **(b)**

Figure D.4: *a)IQ map of dilatometer sample cooled at* 0,5 °C *per minute, where a lot of abrasive stripes can be seen b)IPF map of dilatometer sample cooled at* 0,5 °C *per minute.*

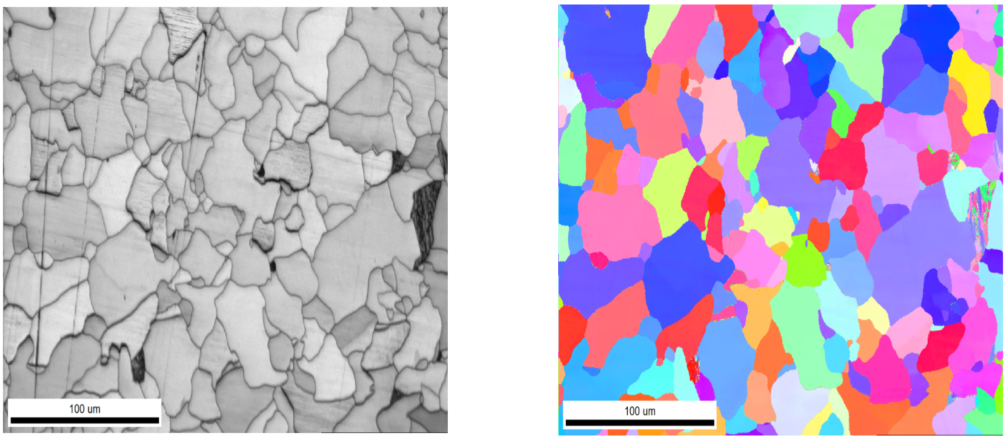

(a) **(b)**

Figure D.5: *a)IQ map of dilatometer sample cooled at* 0,5 °C *per minute. b)IPF map of dilatometer sample cooled at* 0,5 °C *per minute.*

Appendix E

BSE images of dilatometer specimens

E.1 P1d

Figure E.1 to Figure E.10 represent BSE images with different magnification of the dilatometer sample cooled at 5 °C per minute, called P1d in the images below.

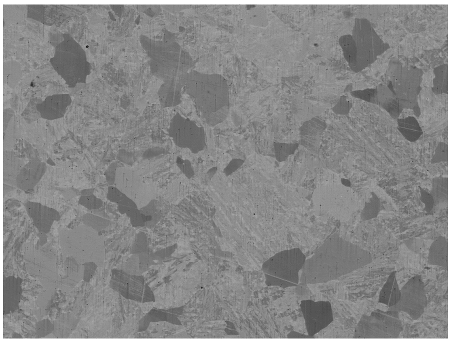

Figure E.1: *Image of P1d at 200X magnification.*

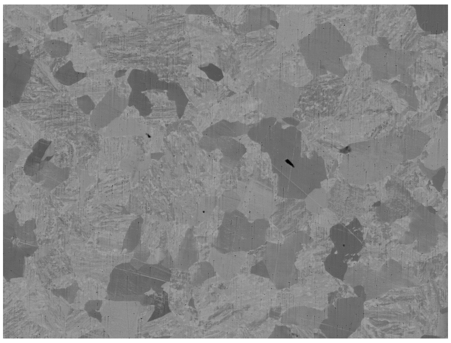

Figure E.2: *Image of P1d at 500X magnification.*

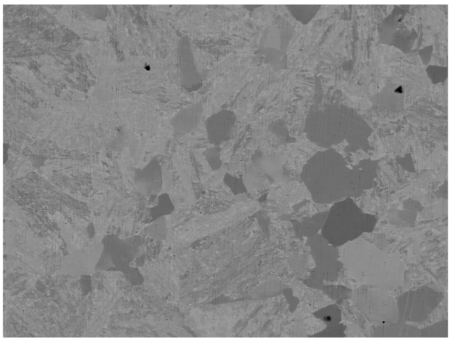
Figure E.3: *P1d at 500X magnification.*

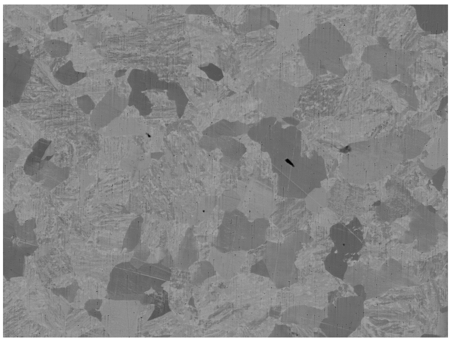
Figure E.4: *P1d at 500X magnification.*

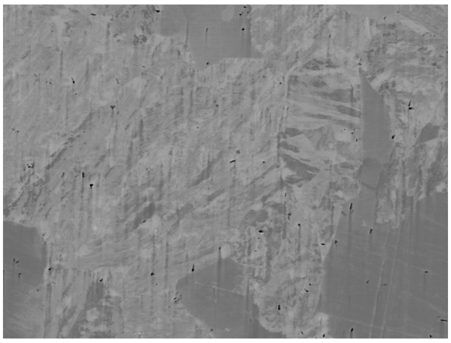
Figure E.5: *P1d at 2000X magnification.*

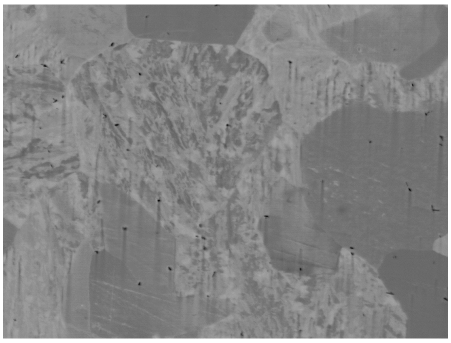
Figure E.6: *P1d at 2000X magnification.*


Figure E.7: *P1d at 5000X magnification.*

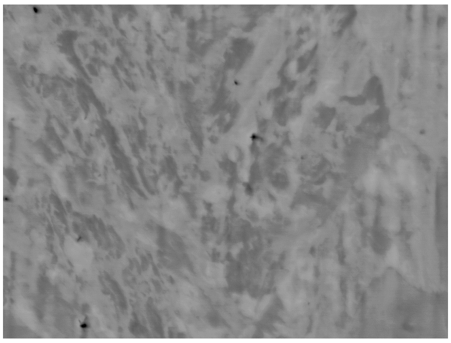
Figure E.8: *P1d at 5000X magnification.*

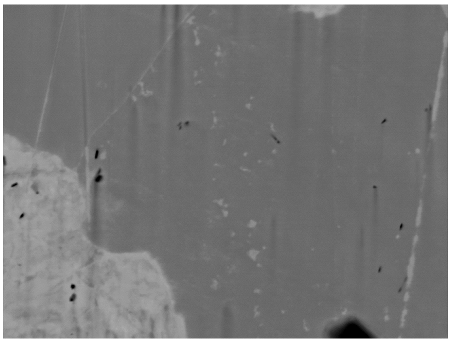

Figure E.9: *P1d at 5000X magnification.*

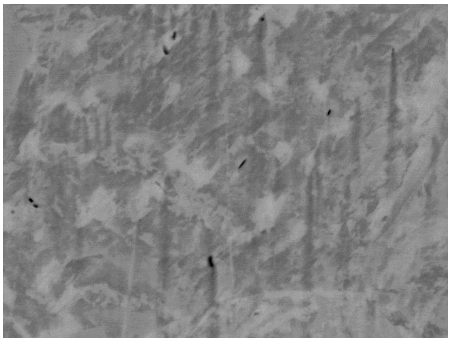

Figure E.10: *P1d at 5000X magnification.*

E.2 P2d

Figure E.11 to E.16 represent BSE images with different magnification of the dilatometer specimen cooled at 1 °C per minute. The sample is called P2d in the figures below.

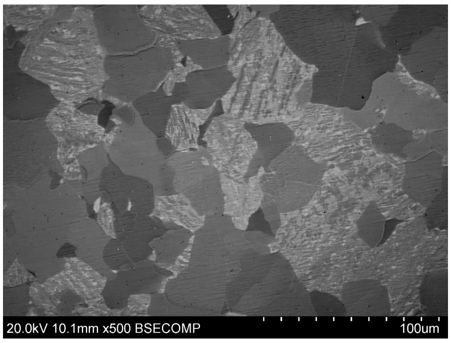

Figure E.11: *P2d at 500X magnification.*

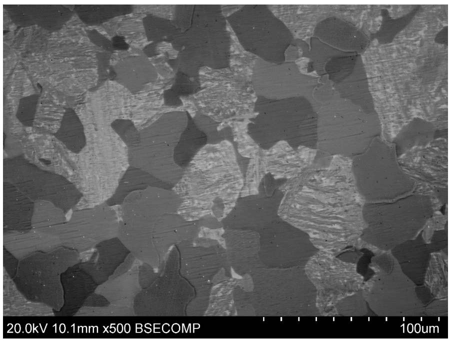

Figure E.12: *P2d at 500X magnification.*

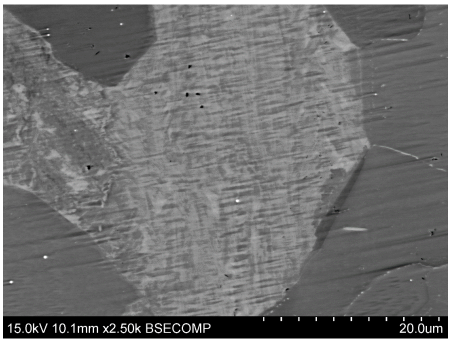

Figure E.13: *P2d at 2500X magnification.*

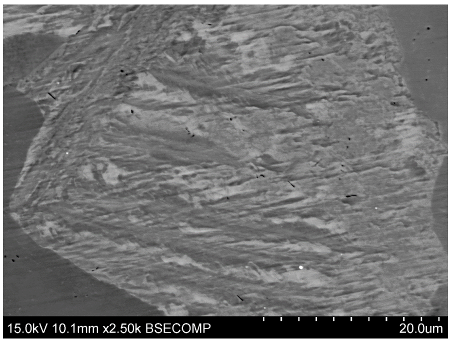

Figure E.14: *P2d at 2500X magnification.*

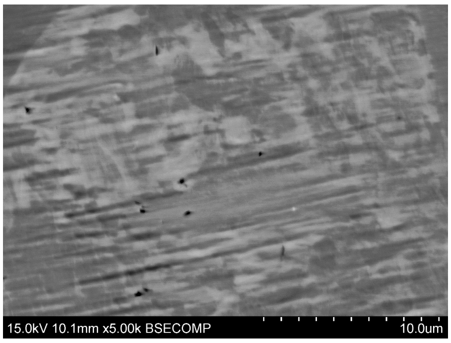

Figure E.15: *P2d at 5000X magnification.*

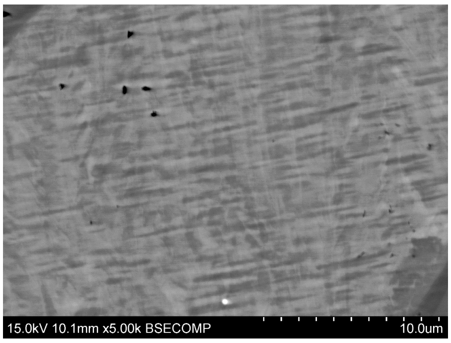

Figure E.16: *P2d at 5000X magnification.*

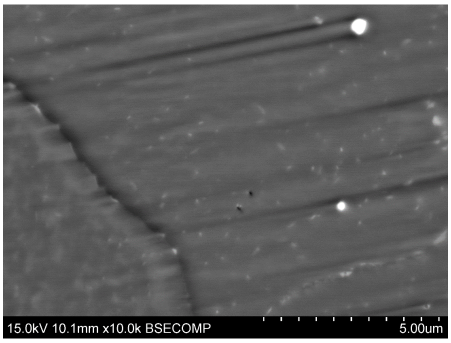

Figure E.17: *P2d at 10000X magnification.*

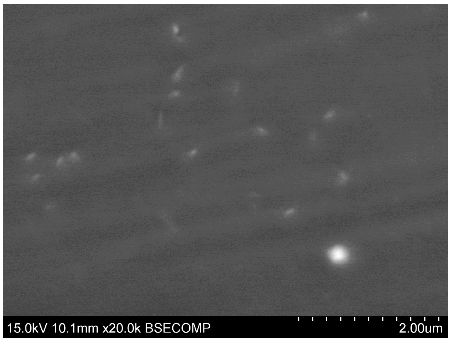

Figure E.18: *P2d at 20000X magnification.*

E.3 P3d

Figure E.19 to Figure E.26 represent BSE images with different magnification of the dilatometer sample cooled at 0, 5 °C per minute. The sample is called P3d in the figures below.

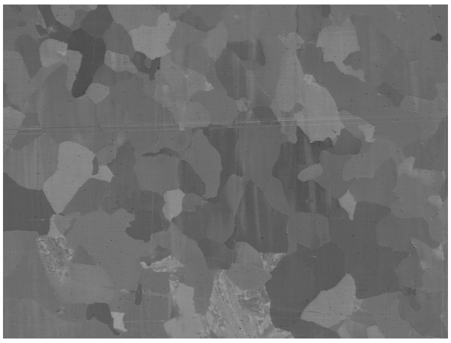

Figure E.19: *P3d at 500X magnification.*

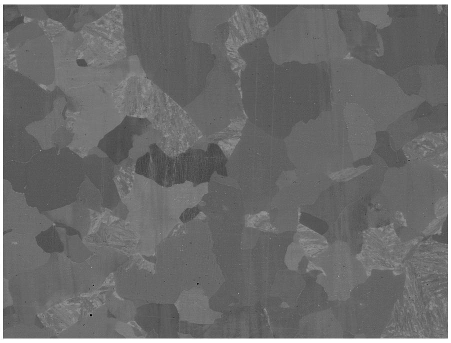

Figure E.20: *P3d at 500X magnification.*

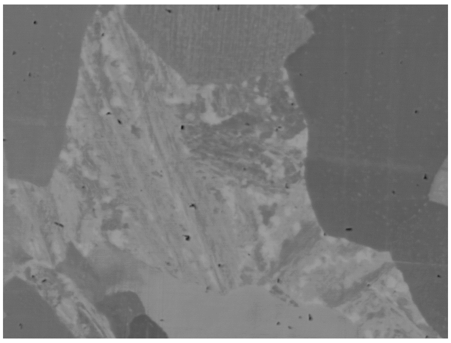

Figure E.21: *P3d at 2000X magnification.*

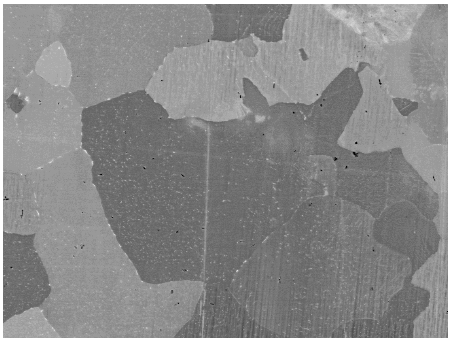

Figure E.22: *P3d at 2000X magnification.*

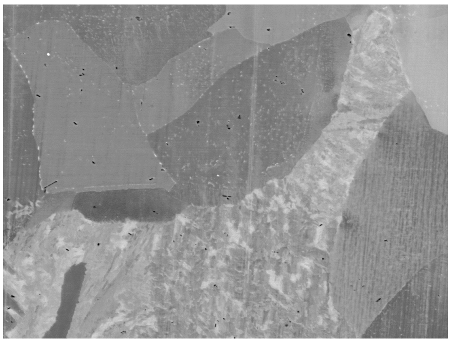

Figure E.23: *P3d at 2000X magnification.*

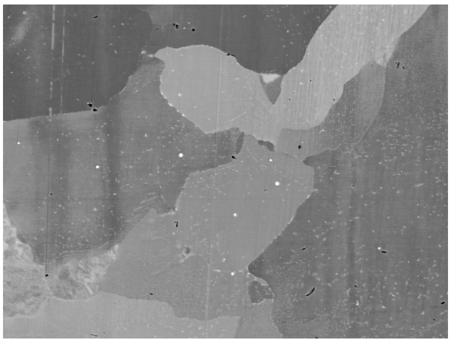

Figure E.24: *P3d at 2000X magnification.*

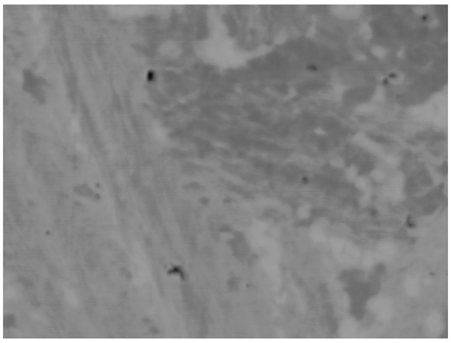

Figure E.25: *P3d at 5000X magnification.*

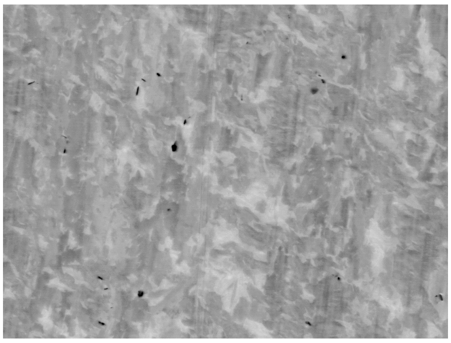

Figure E.26: *P3d at 5000X magnification.*

Appendix F

Tensile Tests

Figure F.1 and F.2 represent the stress strain curves for two of the tensile test specimens. The third curve can be found in section 4.2.1 of the results. The tensile and yield strength for Figure F.1 was found to be 782 MPa and 714 MPa resspectively. The tensile strength for F.2 was found to be 782 MPa and the yield strength was found to be 709 MPa.

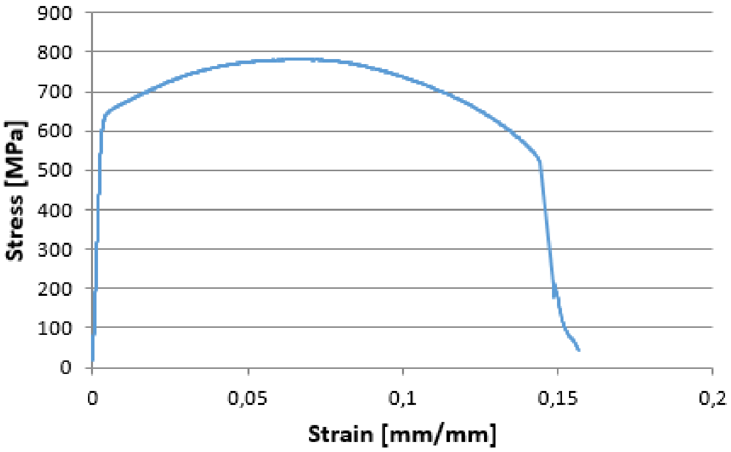

Figure F.1: *Stress strain curve for base material.*

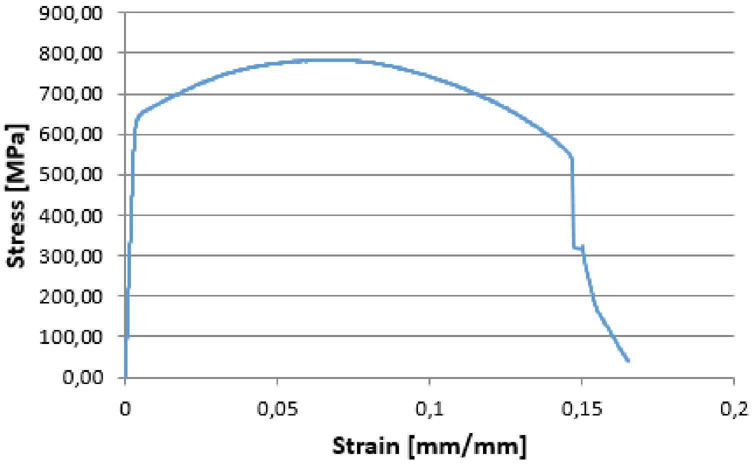

Figure F.2: *Stress strain curve for base material.*

Appendix G

Hardness values

In Table G.1 the hardness values for the dilatometer specimens can be seen. The sample cooled at 5 °C per minute are called P1d, the sample cooled at 1 °C per minute P2d and the sample cooled at 0, 5 °C per minute P3d.

In Table G.2 the Vickers hardness values for the base material are represented.

Table G.1: *Vickers hardness values for dilatometer specimens.*

	Parallel 1	*Parallel 2*	*Parallel 3*
P1d	279 HV5	266 HV5	266 HV5
P2d	175 HV5	175 HV5	188 HV5
P3d	172 HV5	152 HV5	169 HV5

Table G.2: *Vickers hardness values for base material*

Parallel 1	*Parallel 2*	*Parallel 3*
249 HV5	250 HV5	242 HV5
241 HV5	242 HV5	246 HV5
244 HV5	238 HV5	248 HV5
241 HV5	240 HV5	242 HV5
239 HV5	249 HV5	245 HV5
255 HV5	241 HV5	241 HV5
238 HV5	244 HV5	245 HV5
252 HV5	241 HV5	249 HV5
242 HV5	254 HV5	238 HV5
240 HV5	245 HV5	249 HV5
238 HV5	252 HV5	258 HV5
240 HV5	245 HV5	241 HV5
247 HV5	247 HV5	242 HV5
244 HV5	252 HV5	244 HV5
241 HV5	238 HV5	248 HV5
252 HV5	243 HV5	249 HV5
257 HV5	245 HV5	244 HV5
252 HV5	248 HV5	243 HV5
246 HV5	253 HV5	247 HV5
254 HV5	252 HV5	241 HV5

Appendix H

Standard Deviation

The equation used for calculating standard deviation is presented below.

$$\sigma = \sqrt{\frac{1}{N}\sum_{i=1}^{N}(x_i - \mu)^2} \tag{H.1}$$

Where μ is:

$$\mu = \frac{1}{N}\sum_{i=1}^{N} x_i \tag{H.2}$$

Bibliography

[1] NORSOK M 001. Materials selection. `http://www.standard.no/en/PDF/FileDownload/?redir=true&filetype=Pdf&item=132354&category=4`, 2004.

[2] Harshad KDH Bhadeshia. Diffusional formation of ferrite in iron and its alloys. *Progress in Materials Science*, 29(4):321–386, 1985.

[3] Harshad Kumar Dharamshi Hansraj Bhadeshia. *Bainite in steels.* Inst. of Metals, 1992.

[4] H.K.D.H. Bhadeshia. Interpretation of the microstructure of steels. `http://cml.postech.ac.kr/2008/Steel_Microstructure/SM2.html`.

[5] Y Chen, J Hjelen, SS Gireesh, and HJ Roven. Optimization of ebsd parameters for ultra-fast characterization. *Journal of microscopy*, 245(2):111–118, 2012.

[6] J.R Davis. *Metals Handbook*, volume 20. ASM international, 1997.

[7] RA Grange. Estimating the hardenability of carbon steels. *Metallurgical Transactions*, 4(10):2231–2244, 1973.

[8] Anthony Rollett Gregory Rohrer Harry Chien, Bassem El-Dasher. Understanding the tsl ebsd data collection system. `http://www.material.ntnu.no/ebsd/EBSD/OIM-acquisition-guide-6Nov09.ppt.`, 2014.

[9] Jarle Hjelen. *Scanning elektron - mikroskopi.* Metallurgisk institutt, NTH, 1989.

[10] Jarle Hjelen. Electron backscatter diffraction - ebsd in sem, 2013. Power Point presentation in the subject TMT4300.

[11] Robert William Kerr Honeycombe and Harshad Kumar Dharamshi Hansraj Bhadeshia. *Steels: microstructure and properties.* E. Arnold, 1981.

[12] Oxford Instruments. Automated indexing and orientation measurement. `http://ebsd.com/index.php/ebsd-explained/basics-of-ebsd/pattern-formation`, 2013.

[13] KJ Irvine and FB Pickering. Physical properties of martensite and bainite. *Iron and Steel Institute Special Report*, 93:110–125, 1965.

[14] Thomas C Isabell, Paul E Fischione, Catherine O'Keefe, Murat U Guruz, and Vinayak P Dravid. Plasma cleaning and its applications for electron microscopy. *Microscopy and Microanalysis*, 5(2):126–135, 1999.

[15] A Kamada, N Koshizuka, and T Funakoshi. Effect of austenite grain size and c content on the substructure and toughness of tempered martensite and bainite. *Trans. Iron Steel Inst. Jpn.*, 16(8):407–416, 1976.

[16] Sanghoon Lee, Hyesung Na, Byunghoon Kim, Dongjin Kim, and Chungyun Kang. Effect of niobium on the ferrite continuous-cooling-transformation (cct) curve of ultrahigh-thickness cr-mo steel. *Metallurgical and Materials Transactions A*, 44(6):2523–2532, 2013.

[17] Matthew M Nowell and Stuart I Wright. Orientation effects on indexing of electron backscatter diffraction patterns. *Ultramicroscopy*, 103(1):41–58, 2005.

[18] OneSubsea. Deepwater greenfield developments. `http://www.onesubsea.com/integrated_solutions/subsea_provinces_challenges/deepwater_greenfield_developments.aspx`, 2013.

[19] Frederick Brian Pickering. *Physical metallurgy and the design of steels*, volume 63. Applied Science Publishers London, 1978.

[20] PCM Rodrigues, EV Pereloma, and DB Santos. Mechanical properities of an hsla bainitic steel subjected to controlled rolling with accelerated cooling. *Materials Science and Engineering: A*, 283(1):136–143, 2000.

[21] L Ryde. Application of ebsd to analysis of microstructures in commercial steels. *Materials Science and Technology*, 22(11):1297–1306, 2006.

[22] Adam J Schwartz. *Electron backscatter diffraction in materials science.* Springer, 2009.

[23] Jan Ketil Solberg. *Teknologiske metaller og legeringer.* Norwegian University of Science and Technology, 2011.

[24] Struers. Active oxide polishing suspensions, 2014.

[25] K.E. Thelning. *Steel and its heat treatment.* Butterworths, 1984.

[26] George F Vander Voort. *Atlas of time-temperature diagrams for irons and steels.* ASM international, 1991.

[27] Jinghui Wu, Peter J Wray, Calixto I Garcia, Mingjian Hua, and Anthony J DeArdo. Image quality analysis: a new method of characterizing microstructures. *ISIJ international*, 45(2):254–262, 2005.

[28] S Zaefferer, P Romano, and F Friedel. Ebsd as a tool to identify and quantify bainite and ferrite in low-alloyed al-trip steels. *Journal of microscopy*, 230(3):499–508, 2008.

[29] Kangying Zhu, David Barbier, and Thierry Iung. Characterization and quantification methods of complex bcc matrix microstructures in advanced high strength steels. *Journal of Materials Science*, 48(1):413–423, 2013.

[30] Kangying Zhu, Carla Oberbillig, Céline Musik, Didier Loison, and Thierry Iung. Effect of b and b+ nb on the bainitic transformation in low carbon steels. *Materials Science and Engineering: A*, 528(12):4222–4231, 2011.